2005

The investigation of the toughness of a Ni-based alloy with Gd enrichment for spent nuclear waste containment systems

Michael J. (Joseph) Minicozzi
Lehigh University

Minicozzi, Michael J.

The Investigation of the Toughness of a Ni-Based Alloy with Gd Enrichment for Spent Nuclear...

September 2005

The Investigation of the Toughness of a Ni-Based Alloy with Gd Enrichment for Spent Nuclear Waste Containment Systems

by:

Michael J. Minicozzi

A Thesis

Presented to the Graduate and Research Committee

in Candidacy for the Degree of

Masters of Science

in

Materials Science and Engineering

Lehigh University

July 13, 2005

This thesis is accepted and approved in partial fulfillment of the requirements for the Master of Science.

7-13-05
Date

(Dr. John DuPont (Thesis Advisor)

Slade Cargill (Chairperson of Department)

Acknowledgements

I would like to thank my advisor, Dr. John DuPont, for the opportunity to work on a great project in the EMG. I have learned a great deal in the past two years and this would not have been possible without his support and guidance. Also, I would like to thank the NSNFP for their financial support to make this work possible.

Thanks to Dr. Arnold Marder and my fellow EMG members – Weiping Lui, Jon Regina, Matt Perricone, Rick Noecker, Ryan Deacon, Shane Para, Ken Adams, Tim Anderson, Matt Galler, Joe Murphy, and Jeff Farren. The days were extraordinarily memorable (to say the least). Gooo-bye Dr. Marder.

A special thanks to Arlan Benscoter and Mike Rex at Lehigh University. Arlan is the master of metallography and I have learned a tremendous amount from him. Thanks to Mike Rex for machining all my samples and deeming my material the worst material he has ever machined. I would also like to thank Charles Robino at Sandia National Laboratory for all his time and expertise. Thanks to Mark Reece at Sandia National Laboratory for all his help with the shear tests.

To my family, friends, and girlfriend, thank you for all of the encouragement and love you have given me throughout these past two years. I could not have asked for better support.

Table of Contents

List of Tables

List of Figures

1. Abstract

Gadolinium has one of the highest neutron absorption cross sections among the elements and is the most efficient material for criticality control in the U.S. Department of Energy standardized spent nuclear waste canister. An investigation of the toughness of a Ni-Gd-Cr-Mo alloy for spent nuclear waste containment systems is currently underway [1]. The results of this research will lead to the development of a nickel-based alloy for safe transportation and storage of spent nuclear fuel in the Yucca Mountain storage facility in Nevada.

The microstructure of this Ni-Gd-Cr-Mo alloy consists of an austenite matrix that is Ni rich and a eutectic-type constituent consisting of Ni_5Gd and austenite. The Gd rich second phase (Ni_5Gd - gadolinide) is the leading cause of the low ductility and toughness that this material exhibits. The fracture process of these alloys initiates with the cracking of the gadolinides until microcracks are formed, continues with the coalescence of these microcracks, and terminates with fracture. It is this fracture process that facilitated an understanding of why the ingots and hot-rolled plates of this alloy generally showed that the ductility and impact properties are inversely proportional to the concentration of Gd. The quantitative analysis of the gadolinide characteristics showed that as the area percent of gadolinides in the crack propagating plane increased, the mean free path between gadolinides became smaller, and as the aspect ratio of the gadolinides increased that the ductility and impact properties decreased. All of these decrease the impact properties and ductility of this alloy because these characteristics of the gadolinides do not allow for

a great amount of energy absorption prior to fracture. A higher area percent of gadolinides in the crack propagating plane creates more crack initiation sites, gadolinides with large aspect ratios increase the probability of cracking, and smaller mean free paths between the gadolinides lead to easier microcrack coalescence. However, the fracture toughness values of the Ni-Gd-Mo-Cr alloys infer that these materials are tougher than the Charpy impact energies display.

2. Introduction

It has been shown [2] that the fracture process of hard particles in a ductile matrix generally consists of four events: shearing of the matrix, particle cracking and/or particle/matrix decohesion, microcrack formation and growth, and the local linkage of these microcracks. When and how these stages occur determines the properties of an alloy. Therefore, the toughness and ductility of a metal or alloy highly depends upon the characteristics of the second phase particles to resist cracking and avoid a high extent of local linkage of microcracks or crack propagation. If there is great resistance to particle cracking and/or particle decohesion and the distribution of the particles is not clustered, then the material will display high toughness and ductility [2, 3]. The four most important aspects are the size, shape, distribution of the particles, and the interfacial strength of the particle/matrix.

Fundamentally, the fracture process of hard particles in a ductile matrix is dependent upon the local pile-up stresses on the particles from dislocations. The

size, shape, and distribution of these particles are the main factors that control multiple slip band dislocation pileups. Smaller and spherical particles reduce the amount of multiple slip-band pileups that occur because dislocations can cross slip around them more easily. Also, larger particles tend to have bigger and more defects associated with them, which increases the probability of cracking as well [4]. Spherical particles resist particle fracture because they avoid stress concentrations that increase the stress within the particle locally. On the other hand, particles with high aspect ratios are more likely to see multiple slip-band pileups than spherical particles because it is more difficult for a dislocation to cross slip around them. Generally, dislocations do not 'sense' the stress field in the matrix created by an elongated particle until they are too close to cross-slip around the particle and they pile up. Also, as the particle becomes plate-like, the interfacial area between the particle and matrix gets larger producing more tensile stress within the particle because cross-slip becomes harder, thus decreasing the probability that the particle will crack [3]. Finally, the bond between the particle and matrix is also extremely important. Well-bonded particles to the matrix help avoid microvoid formation from decohesion and premature microvoid coalescence. Thus, these particle characteristics avoid local pile up stresses (reduce particle cracking) and increase toughness.

In order to increase toughness even further the particles should be spaced as far as possible from each other to decrease the overlap of stress fields as the material is deformed. Overall, this decreases the particle stress and diminishes particle

cracking probability as well as lengthens the distance microcracks need to link together, which contributes to good energy absorption prior to fracture. Ultimately, clustered particles reduce dislocation motion more effectively than homogeneously distributed particles because if dislocations cross slip away from a particle, they will likely slip into a particle that is in extremely close proximity and eventually get stuck. This leads to higher stresses in these areas, higher particles stresses, and thus higher probability for particle cracking. In effect, if the particles have multiple slip band pileups and a large extent of stress field overlap due to particle clustering, then the toughness of a metal or alloy will be adversely affected because there is small resistance to particle fracture and an ease of microcrack local linkage both leading to a more rapid final fracture.

Moreover, the coherency of the particles with the matrix is an issue. Semi-coherent and incoherent particles are highly favored because coherent particles would be able to be cut by the dislocations introducing planar slip and large dislocation pile-ups. On the other hand, semi-coherent and incoherent particles are usually associated with impenetrable particles allowing for reduced slip distances and a reduction in the number of dislocations sustained in a pile-up [3, 4].

In prior work [5] done on stainless steels containing small amounts of gadolinium, the large melting temperature range (360 to 400°C) and low liquation temperature (1060°C) of the intermetallic $(Fe,Ni,Cr)_3Gd$ proved to be a major problem. Ultimately, this causes liquation cracking during the hot working process and solidification cracking during the welding process. Remedies for these problems

did not work, including heat treatment of the material to promote dissolution of the low temperature intermetallic $(Fe,Ni,Cr)_3Gd$ to a higher temperature phase $(Fe,Ni)_{17}Gd_2$. Therefore, a different alloying strategy had to be investigated. The observation made based on the Ni-Gd phase diagram displayed high temperature eutectic reactions that could replace the peritectic reaction involving the low temperature $(Fe,Ni,Cr)_3Gd$ phase. This could potentially decrease the solidification range and greatly improve weldability and hot ductility. To accomplish this task there would have to be an increase in the nominal content of nickel in the matrix. This idea was tested and improvements were observed on a Ni-Mo-Cr based alloy enriched with 2% concentration of Gd [1]. Differential Thermal Analysis (DTA), hot ductility tests, and fusion welding experiments confirmed that this higher temperature eutectic constituent and smaller solidification range improved solidification cracking resistance and hot workability. However, this material does not exhibit the optimal ductility and toughness that is desired of these alloys for transportation and storage applications.

In order to understand the mechanical properties that the Ni-Gd-Mo-Cr alloys are exhibiting one must understand the microstructure of the material. The microstructure consists of an austenite matrix that is Ni rich and a eutectic-type constituent consisting of Ni_5Gd and austenite. The main concern lies within the brittle nature of the Ni_5Gd. In the Ni-Gd-Mo-Cr ingots the Ni_5Gd within the eutectic is brittle and distributed throughout the matrix in clusters. Additionally, the distribution, size, and shape of a brittle second phase within a ductile matrix have a

significant impact on its fracture process and properties [2]. Therefore, the main objective of this research is to determine the influence of Gd additions on the tensile and impact properties of a Ni-Mo-Cr alloy. The results of this research will be useful for future alloy optimization endeavors.

3. Experimental Procedure

3.1 Ingot casting

Eight Ni-Gd-Mo-Cr ingots were vacuum cast at Santoku America Inc. in Tolleson, Arizona. The dimensions of each ingot were 14 inches long with a square base of 4 inches. The compositions of these ingots can be seen in Table I. The first six alloys shown in Table I have a range of nominal Gd concentrations between 0 and 2.5 wt%. It was this range of concentrations that were investigated to show the relation between the Ni_5Gd content and the mechanical properties of the alloys. The last two alloys both have approximately 2-wt% Gd, but also include B concentrations of 230 ppm and 510 ppm, respectively. The B was added in attempt to increase the ductility and toughness by changing the distribution and characteristics of the Ni_5Gd.

3.2 Hot Rolling schedule

All of the ingots were hot rolled at 2200°F. They were kept at this temperature for sixteen hours prior to rolling and hot rolled from 4 inches to 1 inch with each pass reducing the material by 0.5 inches. After each inch of reduction the samples were reheated to 2200°F for four hours. The samples were then air-cooled

and cut in half. After four hours at 2200°F the samples were hot-rolled again. One half of the sample was cross-rolled (CR) (rolled perpendicular to primary rolling direction) from 1 inch to 0.5 inches in two passes and the other was straight-rolled (SR) (rolled in the primary rolling direction) with the same procedure. Finally, the samples were annealed at 2200°F for four hours and water quenched.

3.3 Metallographic Procedure

Each of these ingots and plates were prepared metallographically. Three samples were cut with an abrasive wheel and mounted in Buehler epoxicure resin to investigate all three directions of the ingots and rolled plates. The samples were ground to 600 grit and polished to 0.05μm colloidal silica. Finally, the samples were etched with Beraha 7A solution consisting of 1g sulfamic acid, 3g potassium metabisulfite, and 100ml distilled water. Micrographs of the mounted samples were taken on a Nikon light optical microscope interfaced with PaxIT imaging software.

The Princeton Gamma Tech (PGT) software was used to determine the aspect ratio, size, mean free path, and area percent of the Ni_5Gd second phase. In order to use this software and do this particular analysis, a bitplane of the second phase in the microstructure was created using the LECO IA-3001 software. A bitplane is created by making a threshold of the second phase based on the grayscale of a micrograph. A threshold is made from all the gray pixels that make up the second phase.

3.4 Mechanical Testing

Tensile and Charpy Impact testing were performed on all ingots and rolled plates. Charpy impact testing was conducted at room temperature in accordance with ASTM Standard E23 [6] on type A Charpy bars in the T-L and L-T orientations. The impact energy, lateral expansion, and shear percentage were all recorded. The samples for tensile testing were round sub-size tension specimen with a 0.250-inch nominal diameter and a gage length of 1 inch. Tests were done at room temperature in accordance with ASTM Standard E8 [7] on orientations that were transverse and longitudinal to the rolling direction. Recorded measurements include yield strength, ultimate tensile strength, reduction in area, and elongation.

Tensile tests were also conducted on rolled plates of a borated stainless steel 304B4B (BSS) and a Ni-Gd-Mo-Cr alloy (composition shown in Table II) in accordance with ASTM Standard E8 [7] to understand the fracture process of a brittle phase in a ductile matrix. Five round sub-size tension samples with a 0.250-inch in nominal diameter and gage length of 1 inch from each material were tested transverse to the rolling direction. The first sample was tested until failure to determine the correct crosshead displacement for the other four samples that were plastically strained 2, 4, 6, and 8%. The crosshead speed was 0.1 inches per minute. All five samples were prepared metallographically and examined in the as-polished condition to accentuate the second phase in the microstructure. The tensile specimens were examined along the entire gauge length perpendicular to the loading direction. In addition, microhardness measurements were taken on the second

phases of both the borated stainless steel 304B4B (BSS) and a Ni-Gd-Mo-Cr alloy in accordance with ASTM Standard E92 [8]. A LECO ACP-94 Computing Printer with an Optical shaft encoder type TS1702 was used in conjunction with a LECO M-400FT Hardness Tester. Vickers indents were used at 1g for 10 seconds.

Fracture toughness testing was conducted on one Ni-Gd-Mo-Cr alloy (composition shown in Table III) using a compact tension sample having a width of 2 inches and a thickness of 0.5 inches. Two samples of both the CR and SR material were tested. The samples were machined in the T-L orientation from both cross-rolled (CR) and straight-rolled (SR) material (procedure mentioned previously). Testing was performed in accordance with the ASTM E 1820-01 "Standard Test Method for Measurement of Fracture Toughness" [9]. A single specimen unloading compliance technique was used to monitor stable crack extension. The tests were conducted on a 20,000 lb. MTS servo-hydraulic mechanical test system using an MTS 458 controller interfaced to an Adwin-Gold FTA computer system and configured for fracture toughness testing. An MTS model 632.03B-30 clip gage was used for load-line displacement measurement. Standard 1.0T compact tension clevises with flat-bottom holes were used to transfer force from the load train to the test specimen.

During this fracture toughness test, the specimen was loaded to a certain load and displacement level and the load was reduced approximately 10%. The specimen compliance was measured during this unloading period and the crack length could be determined for this particular compliance value. The J value could also be calculated

using particular areas under the curve. During the same test, this was done numerous times creating an R-curve (J vs. Δa) where the J_{IC} was determined. K_{IC} was then determined from J_{IC} using this equation (plane stress condition):

$$K_{IC} = \sqrt{J_{IC} E}$$

where E is the elastic modulus [10].

4. Results

4.1 Microstructural Characterization

The Ni-Gd-Mo-Cr alloy microstructure consists of primary hypoeutectic γ austenite phase that is nickel-rich and a eutectic-type γ/Ni_5Gd constituent. The solidification behavior and microstructural development of these alloys have been discussed previously by DuPont et.al. [1]. Figure 1a and 1b displays photomicrographs taken from a Light Optical Microscope (LOM) of a Ni-Gd-Mo-Cr alloy in the cast condition with 1.90 wt% Gd where the austenite matrix γ and γ/Ni_5Gd eutectic-type constituent are labeled. The SR and CR counterpart evolved microstructures can be seen in Figure 1c and 1d, respectively. Both rolling schedules almost completely broke-up the eutectic morphology. The SR procedure elongated the γ/Ni_5Gd constituent while the CR plates showed that the texture created by the straight rolling procedure was alleviated by cross rolling.

The microstructures of the Ni-Gd-Mo-Cr alloys with 230 ppm of B are shown in Figure 2. There were two main differences in the microstructure of the B-containing alloys. The first was the eutectic morphology was not well defined. This

type of growth where the components of a eutectic are entirely separated is described as divorced. The second was that another eutectic constituent shown in Figure 2a and 2b was present that "webs" between the Ni_5Gd phase. Tentative phase identification with Electron BackScatter Diffraction (EBSD) indicated that the second phase within the eutectic was based on a molybdenum boride. Figure 2c and 2d displays texture features similar to the B-free alloys, except that the gadolinides appear to be spaced farther apart. The hot-rolled plates with 510 ppm of B were extremely similar in microstructure to the plate with 230 ppm, but there was a higher area fraction of the B rich phase.

4.2 The Fracture process - Comparison between a Borated Stainless Steel and Ni-Gd-Mo-Cr alloy

Borated stainless steel 304B4B (BSS) is an alloy that was used in a comparison with a Ni-Gd-Mo-Cr alloy to better understand how the second phase affects the failure mechanism of each material. The character of these two materials is qualitatively similar. The microstructures of both these alloys are hard particles in a ductile matrix. Robino and Cieslak concluded that the BSS microstructure consists of chromium boride precipitates (Cr_2B-type) in an austenitic stainless steel matrix [11]. The longitudinal impact energy versus the area fraction of the chromium boride precipitates using both Grade A and Grade B BSS material may be seen in Figure 3 [12]. Grade A and Grade B are classifications for the particular processing of the alloys. Grade A is powder metallurgy ingot-hot work processing and Grade B is

conventional ingot metallurgy. The particular area fraction of Cr_2B particles in the BSS alloy tested in this study was 0.16 and from Figure 3 the impact energy in the longitudinal direction to rolling was approximately 35 ft-lb. Comparing this to the Ni-Gd-Mo-Cr alloy tested, the area fraction of the gadolinides was 0.01 and the longitudinal impact energy was approximately 24 ft-lb. Tensile tests were conducted to determine why the BSS has a greater impact energy and how the nature of the particle cracking and deformation affected the fracture process.

The Ni-Gd-Mo-Cr alloy and the BSS tensile specimen were compared in two ways. The first was how the second phase of the BSS and Ni-Gd-Mo-Cr alloy was affected by the plastic strain at the middle of the gauge length (where strain was known exactly) and the second was comparing the failed specimen directly near the fracture surface. The unaffected rolled plate microstructures of the BSS with chromium boride particles and Ni-Gd-Mo-Cr alloy with the gadolinides are shown in Figure 4 (LOM photomicrographs). Both materials after 2%, 4%, 6% strain, and a failed specimen near the fracture surface are shown in Figure 5 for a direct comparison of the cracking of the second phases.

No cracks were evident in the photomicrographs of the unaffected rolled plate BSS and Ni-Gd-Mo-Cr alloy microstructures (Figure 4). However, in Figure 5, when the specimen were strained plastically to 2% small cracks in the larger chromium boride particles were visible as well as some particles with large aspect ratios (Figure 5a). On the other hand, the Ni-Gd-Mo-Cr alloy had multiple cracks that were already evident in the same types of particles (Figure 5b). As the plastic

strain increased to 4% on the BSS (Figure 5c), not only were the number of cracks greater compared to 2% strain, but multiple cracks were noticeable on individual particles. At this strain the Ni-Gd-Mo-Cr alloy particles were cracked even wider and the smaller and more circular particles were cracked as well (Figure 5d). The LOM photomicrographs of both the Ni-Gd-Mo-Cr alloy and BSS at 6% strain (Figure 5e and f) display that even some of the larger particles in the BSS did not crack, but the larger particles in the Ni-Gd-Mo-Cr alloy at these strains were all heavily cracked along with most of the smaller ones. Also, the applied strain did not cause cracking in the smaller and more circular chromium borides. Clearly, the cracking initiation was highly dependent upon the morphology of the second phase. Particles that were large and had high aspect ratios tended to crack easier than smaller circular particles.

As one examined the specimen in Figure 5 starting from the 2% strain specimen to the failed specimen, the particles cracked first, then the cracks became microcracks and eventually coalesced, and finally the material fractured. The two main differences between the BSS and Ni-Gd-Mo-Cr alloy were the number and size of the cracks present at each strain and that the voids in the failed samples (Figure 5g and h) of the Ni-Gd-Mo-Cr alloy were several times the size of the BSS voids.

4.3 Mechanical Testing

The main objective in this study was to determine how the Gd concentration influences the microstructure of the nickel based alloy and, in turn, how this affects

the mechanical properties. Therefore, each property tested was plotted against the Gd concentration for each alloy.

It is shown in Figure 6 that the Charpy impact energy and elongation decreased gradually as the Gd concentration increased (except the B containing alloys). The ingot values were always less than all of the plate values. Additionally, the results for the SR plates transverse to the rolling direction (T-L for Charpy bars) were lower than the values for the SR plates longitudinal to the rolling direction (L-T for Charpy bars) with all the quantities from the CR plates in between. The CR plate values transverse to the rolling direction were approximately equal to the results longitudinal to the rolling direction. Finally, the alloy with 230 ppm of B generally increased impact energy and elongation slightly. However, as the concentration increases to 510 ppm of B, the properties were generally adversely affected.

The rest of the Charpy impact properties tested are shown in Figure 7 including the lateral expansion and percent shear of the Charpy bars. The same trends generally hold for these properties, except that both alloys with the B concentration slightly improved the lateral expansion and shear.

The ultimate tensile strength (UTS), yield strength, and reduction of area can be seen in Figure 8. The UTS for the plates increased slightly as the Gd concentration increased. The ingot value dropped as Gd was initially added but remained constant as Gd increased. Also, alloys that were enriched with B negatively affected the plate UTS values. Similar trends existed for the yield strength of these alloys. However, the increase in yield strength was more prevalent

and the ingot values increased as a higher concentration of Gd was added. Also, the reduction in area was similar to the elongation shown in Figure 6.

Fracture toughness testing was conducted on a Ni-Gd-Mo-Cr alloy with 1.90 Gd concentration in order to acquire the critical J-integral (J_{IC}), which is a parameter used to describe the fracture conditions in a component undergoing elastic and plastic deformation [13]. The J_{IC} values were then utilized to find corresponding fracture toughness (K_{IC}) values. These results for both the SR and CR plates in the T-L orientation are shown in Table IV. In order to determine J values at particular crack displacement values Δa, load vs. displacement curves were created from the compact tension specimen.

5. Discussion

5.1 Comparison between a Borated Stainless Steel and Ni-Gd-Mo-Cr alloy

In order for one to comprehend the basis of how the different aspects of a second phase influence the mechanical properties of the Ni-Gd-Mo-Cr alloys, the fracture process must be well understood. It was evident from the tensile tests of the Ni-Gd-Mo-Cr alloys and the BSS that the fracture process of these alloys initiates with the cracking of the second phase until microcracks are formed, continues with the coalescence of these microcracks, and terminates with fracture. It was determined that the size and shape of the second phase, in this particular case, played a larger role in the fracture process than its brittle nature because the gadolinides cracked more severely than the chromium borides at low strains. All of this

knowledge was then applied to how the size, shape, and distribution influenced the mechanical properties of the Ni-Gd-Mo-Cr alloys.

The fracture process seen in this study on the Ni-Gd-Mo-Cr alloy and the BSS was the same as research done by *Wang* on A356 and A357 aluminum casting alloys [2]. The microstructure of these alloys consisted of a ductile aluminum matrix with hard Fe-rich and Si eutectic particles. There was no particle/matrix decohesion, therefore a good comparison could be made between the Al alloys and the alloys in this study.

Basically, particles crack because the matrix transfers the load to the particles by shear stresses along the particle/matrix interface, elastically elongating the particles. Eventually the particles cannot bear the load, become unstable, and crack. A greater resistance to particle cracking increases the toughness and ductility of the material by delaying the microcrack coalescence to higher strain values. It was clearly seen in Figure 5 that the extent of the gadolinide cracking at each strain was more severe than the chromium boride cracking. The severity of the gadolinide cracking at much lower strains compared to the chromium borides led to coalescence of the microcracks at lower strain levels and a smaller amount of energy absorption prior to fracture. This accounts for the higher impact energy of the BSS compared to the Ni-Gd-Mo-Cr alloy.

Wang also observed that particles that were larger and had large aspect ratios tended to crack easier than those that were small and more circular. The same observations were made in this study for both the materials. Large, high aspect ratio

particle are more susceptible to cracking due to local pile-up stresses on the particles from dislocations. Particles that are large and have big aspect ratios are more susceptible to multiple slip band dislocation pileups because it is more difficult for dislocations to cross slip around them. Additionally, spherical particles resist particle fracture because they avoid stress concentrations that increase the stress within the particle locally [3, 4].

An important difference between the Ni-Gd-Mo-Cr alloy and the BSS was the brittle nature of their second phases. The hardness value of the gadolinides was 449 ±18.9 Vickers (V) with a matrix hardness of 152 ± 7.40 V, while the hardness of the chromium borides was 874 ± 42.7 V with a matrix hardness of 119 ± 5.90 V. One would assume from these values that the chromium borides would crack before the gadolinides because they are more brittle, but this was not observed. Therefore, the shape of the second phases when comparing these microstructures is more important than their brittle nature. One main factor that increased the cracking probability of the gadolinides that the chromium borides did not possess was large aspect ratios. Qualitatively, it can be seen in Figure 4 that the aspect ratios of the gadolinides are much larger. This may be the main factor contributing to why the gadolinides crack at extremely low strains and the chromium borides do not.

5.2 Qualitative Microstructural Analysis of Ni-Gd-Mo-Cr ingots and plates

3D representations of the ingot and hot-rolled microstructures were created in order to display the microstructure in each direction. These 3D representations were

produced for the ingots and rolled plates with 0.46, 1.01, 1.90 wt% Gd as well as the alloy containing 1.94 wt% Gd and 230 ppm of B. The ingot microstructures are shown, respectively, in Figures 9 to 12. The Charpy and tensile bar orientations are illustrated to show the crack dividing plane (B) and the crack-propagating plane (C).

It was evident from Figures 9 to 12 that, as the Gd concentration increased, four factors could potentially affect the impact and tensile properties of these alloys. These four factors were the area fraction of gadolinides, the gadolinide size, the gadolinide aspect ratio, and the mean free path of the gadolinides. Unless otherwise stated, the gadolinide size was considered to be the area equivalent circle radius (R_{EC}) defined by the following equation:

$$R_{EC} = (A/\pi)^{1/2}$$

where A is the particle area. The mean free path (λ) is defined as the average distance between the surfaces of particles along any random straight line in the microstructure [14, 15]. A schematic of this parameter is shown in Figure 13. The equation for the mean free path is as follows:

$$\lambda = \frac{1 - Vf}{N_L} \tag{1}$$

where V_f is the volume fraction of particles and N_L is the number of particles per unit length on any random line. This equation is applicable to any particle dispersion because it is independent of size, shape, and distribution of particles. The aspect ratio of a particle is defined as the length of the particle divided by the width of the particle. It was clear that these four factors are linked. Qualitatively, a higher area

fraction of gadolinides produced gadolinides with larger particle sizes and aspect ratios and a smaller mean free path.

As shown before, the fracture process of these alloys commences with the cracking of the gadolinides, the formation of microcracks, the coalescence of these microcracks into voids, and final failure. Based on the 3D representations in Figures 9 to 12, the ingots with higher Gd concentration generally have gadolinides with greater aspect ratios and sizes than those with smaller Gd concentration. This increased the probability that the gadolinides cracked [2]. Additionally, these alloys have a smaller mean free path between gadolinides that produced easier coalescence, leading to less amounts of energy prior to fracture and smaller ductility values because a smaller fraction of the tough austenite matrix was confronted by the cracks. Therefore, in addition to the increased area fraction of gadolinides present in the alloys as the Gd concentration increased, the gadolinide aspect ratio and size as well as the mean free path were also key to understanding the decline in the properties mentioned above. Lastly, in Figure 6 it was apparent that the divorced eutectic and B phase did not play such a large role in the impact energy and elongation for the ingot values. There was not much of a difference that would have occurred during the fracture process based on the microstructures seen in Figures 11 and 12.

The presence of the gadolinides was beneficial for the UTS and yield strength of the Ni-Gd-Mo-Cr alloys, except for the ingot UTS values. This was clearly seen in Figure 8. Fundamentally, the reason the yield strength increased was because the

gadolinides are brittle. During elastic deformation, the stress was transferred from the austenite matrix to the gadolinides. The hexagonal closed packed structure of the gadolinides does not have as many slip systems for dislocation motion to begin as the austenite matrix (FCC) does and therefore sustains higher stresses before it plastically deforms. In addition, as the Ni-Gd-Mo-Cr alloys began to deform the UTS also increased because the gadolinides intensified the work hardening of the material by prohibiting dislocation motion and created pile-ups as previously mentioned. Finally, the main reason why the UTS and yield strength values dropped when the Ni-Gd-Mo-Cr alloys were enriched with B may have been due to the larger average spacing between the gadolinides when compared to the Ni-Gd-Mo-Cr alloy with the same Gd concentration and area fraction of gadolinides [16]. Therefore, the Ni-Gd-Mo-Cr alloy without the B has a smaller average spacing between particles that would create more of a stress field overlap from the particles and prohibit dislocation motion more.

The deformation of the Ni-Gd-Mo-Cr alloys from the rolling processes in this study had an influence on the impact energy, elongation, lateral expansion, shear percentage, and reduction in area. These properties were also explained by their 3D representations presented in Figures 14 to 17. Each figure includes the microstructures in each direction for CR and SR plates (including rolling directions) for the same ingots displayed earlier. Illustrations of the T-L and L-T orientations of the Charpy bars show the crack dividing plane, the crack-propagating plane, and the top/bottom of the plate. For the Charpy bars in the T-L orientation, B was the crack-

propagating plane and C was the crack-dividing plane. The L-T orientation switches these two directions around. In other words, for the L-T orientation, C was the crack-propagating plane and B was the crack-dividing plane. Tensile bars were also illustrated to properly orient the reader.

From Figures 6 to 8 the impact properties and ductility values for the plates were always greater than the ingot results. Overall, the ingot microstructures show the greatest gadolinide aspect ratios and sizes and the smallest mean free path when comparing the same Gd concentration level. After hot rolling the ingots, one can see that the eutectic-type structure has almost disappeared and gadolinides have been distributed or broken up attributing from several factors including rolling direction, cross-rolling or straight rolling, etc. This would be the reason why the impact properties and ductility values for all the plates were better than the ingot results.

Also, all impact and ductility values for the SR plates transverse to the rolling direction (T-L for Charpy bars) were always worse than the values for the SR plates longitudinal to the rolling direction (L-T for the Charpy bars). This was explained by looking at each direction of the plate microstructures individually. In each of the SR microstructures shown, the A plane (top of the plate) shows an elongation of the gadolinides in the rolling direction. From this face, one may deduce that a crack through a transverse tensile bar or T-L Charpy bar will propagate easier than a crack through a longitudinal tensile bar or L-T Charpy bar. The B plane of all the SR microstructures displays gadolinides that are more elongated with a smaller mean free path for the propagation of a crack than the C plane. Therefore, lower impact

properties and smaller ductility values were associated with transverse tensile bars or T-L Charpy bars compared to longitudinal tensile bars and L-T Charpy bars.

Equally as important was that the CR values transverse to the rolling direction were approximately equal to the results longitudinal to the rolling direction. The cross rolling developed an isotropic nature and did not allow for the mean free path and aspect ratio of the gadolinides in one particular direction to be as severe as straight rolling. In other words, the cross rolling alleviated the anisotropic nature of the SR plates. The mean free path and gadolinide aspect ratios were also not as severe in any particular direction, which created results that were in between those of the SR plates.

Finally, the B-containing alloy with 230 ppm exhibited a slightly increased impact energy and elongation compared to the alloy with the same concentration of Gd. Figure 16 in direct comparison to Figure 17 provided the explanation that the deformed gadolinides were more separated from one another, which ultimately raised the impact energy and elongation. However, the gadolinides were larger and possibly have higher aspect ratios, so this alloy did not produce a significant increase in these properties. As the concentration of B increased to 510 ppm the properties were adversely affected. Therefore, B seems to be helpful with respect to impact energy and elongation only to a certain extent. It is shown in Figure 18 comparing the two alloys with B that there was a significant increase in the amount of the B rich phase in the alloy with a higher concentration of B. So, the cause of the reduction of these properties was possibly due to the higher area fraction of the B rich phase.

Ultimately, the reason behind this is that a higher area fraction of this B rich phase leads to more crack initiation sites and facilitates crack coalescence.

5.3 Relationship among particle size, volume fraction, and mean free path

There is a relationship among the size of the particles, the volume fraction, and the mean free path between the particles. This relationship was derived from Equation 1 for the mean free path between particles. Equation 1 can be manipulated using the average particle intercept length (L_3) and rearranged into the following equation:

$$\lambda = \overline{L_3}(\frac{1}{V_f} - 1) \tag{2}$$

where L_3 is defined as the average length of any line passing through the particle, randomly, on any plane section [15]. L_3 can be seen in Figure 13 of the schematic of the mean free path. If the particles are of uniform size, then this parameter changes based on the shape of the particles. Theoretically, if a microstructure consists of a phase of particles with uniform spheres of radius (r), then L_3 is 4/3 times the radius of those particles making Equation 2 become [14, 15]:

$$\lambda = \frac{4r}{3}(\frac{1}{V_f} - 1) \tag{3}.$$

Also, if a microstructure of a phase of particles that are randomly oriented rods of radius r and length H, where H >> r, then L_3 is 2 times the radius of those particles making Equation 2 become [14, 15]:

$$\lambda = 2r(\frac{1}{V_f} - 1) \quad (4).$$

So, the calculated mean free path from these equations and the experimental mean free path from the PGT software were compared to better understand and classify the relationship between the volume fraction of gadolinides, the size of the gadolinides, and the edge-to-edge distance between them. The calculated and measured mean free path values came from the B and C planes of the rolled plates. The mean free path values using Equations 3 and 4 were calculated using the experimentally determined area fraction, and the mean R_{EC} or half the mean fiber width (to represent the radius of the rods) of the gadolinides, respectively. The following graph shown in Figure 19 are the calculated mean free path values versus the measured mean free path values for each plane of the SR and CR plates (i.e. the B plane in the CR plate is labeled as CRB, etc.). The line in the middle of the graphs represents the theoretical 1:1 line. The results illustrate that generally the sphere data was an underestimate of the theoretical mean free path and the rod data was an overestimate of the theoretical mean free path. Therefore, one would assume that the Ni-Gd-Mo-Cr plate microstructures be classified between these two theoretical limits.

5.4 Quantitative Microstructural Analysis of Ni-Gd-Mo-Cr ingots and plates

The qualitative analysis of the microstructures of the Ni-Gd-Mo-Cr ingots and plates showed four factors that were most important about the characteristics of a brittle second phase in a ductile matrix: the area percent of gadolinides in the crack

propagating plane, the size, the mean free path between gadolinides, and the aspect ratio. Therefore, all of these were intensely studied. Figures 20 through 25 summarize all the quantitative data with plots showing the impact properties and ductility against the area percent, mean free path, and aspect ratio. It is important to note that all data points from these figures come from the crack-propagating plane for a valid comparison between the ingots and rolled plates.

The trends of each particular characteristic were well established. Generally, a larger area percent of gadolinides lowered the impact properties and ductility of the alloys. Also, a smaller mean free path between gadolinides decreased both the impact properties and ductility. Finally, a larger aspect ratio reduced the impact properties and ductility. Each gadolinide characteristic affected the properties above, so they were examined separately as well as together to develop a better understanding of the effects of the hot-rolling schedules on the gadolinides. In addition, aspect ratio histograms for all the ingots and plates were created to further aid in the confirmation of the qualitative analysis.

In all graphs shown in Figures 20 to 25 one established a sense of how the Gd concentration affected the properties. For instance, in Figure 20 the data points (left to right) that are connected correspond to the Ni-Gd-Mo-Cr alloys 2 through 6 in Table I, respectively. So, the Gd concentration was increasing in Figure 20 as the area percent of gadolinides rose. This was similar for Figures 22, 23, and 25 and the reverse for Figures 21, and 24. In other words, a higher area percent, a smaller mean free path, and larger aspect ratio lowered the impact properties and ductility of the

Ni-Gd-Mo-Cr alloys regardless of the rolling schedule as the Gd concentration increased. The data points for the alloy with 230 ppm of B are the points that are not connected. To further clarify the aspect ratio portion of the explanation, Figures 26 and 27 display five aspect ratio histograms. These diagrams exclude the B concentrated alloys. One is the ingot histogram while the others are from the rolled plates for the B and C planes. Generally, it was clear from all of these histograms that as the Gd concentration increased that more of the gadolinides had a large aspect ratio and a lower percentage had a small aspect ratio. This was more obvious in Figure 27.

Figures 20 through 25 were also utilized to confirm why the impact properties and ductility values for the ingots were always less than the results obtained for the rolled plates (Figure 6). In any of the charts with area percent or mean free path of the gadolinides, one can see that at any given area percent or mean free path value that the ingot impact properties and ductility were generally the lowest. This trend was not seen in the charts with the aspect ratio of the gadolinides for the impact properties and ductility, but the aspect ratio histograms for the ingots and plates in Figures 26 and 27 clarified this ambiguity. The ingots produced the highest percentage of the larger aspect ratios for any given Gd concentration. This all confirmed that the hot rolling had a significant effect on the area percentage of the gadolinides in the crack propagating plane, the mean free path, and the aspect ratio of the gadolinides by breaking up the eutectic-type structure.

In addition, this quantitative analysis can prove why the Charpy impact properties and ductility of SR plates transverse to the rolling direction were worse than the SR plates longitudinal to the rolling direction as well as why the CR plate values transverse to rolling were approximately the same as the CR plate values longitudinal to rolling (Figure 6). An argument similar to before was made to explain this observation. In any of the charts with area percent or mean free path of the gadolinides, it was clear that any given area percent or mean free path value that the SR plate impact properties and ductility in the transverse direction to rolling were always worse than the SR plate impact properties and ductility longitudinal to the rolling direction. In these graphs it should also be noted that the CR plate values, regardless of specimen orientation, are approximately equal and lay between the SR plate values. Figures 22 and 25 once again are unclear with respect to this particular analysis. Therefore, aspect ratio histograms were created comparing the distribution of the B plane to the C plane for both the SR plates and the CR plates. These are presented in Figure 28. Clearly, the aspect ratio distributions in the B and C plane for the CR plates are similar which confirmed that, along with approximately the same mean free path and area percent for any given Gd concentration, the cross rolling developed an isotropic nature within the alloys and did not allow for the deformation of the gadolinides in one particular direction to be as severe as straight-rolling.

The SR plate aspect ratio distribution in Figure 28 was different, which was expected. The B plane contained a much larger percentage of gadolinides with big

aspect ratios and a much smaller percentage of gadolinides with small aspect ratios. This validated the examination of the plate microstructures that displayed that the B plane of all the SR microstructures had gadolinides with a higher aspect ratio than the C plane for any given Gd concentration. These microstructures had a larger percentage of gadolinides with a high aspect ratio and at any given concentration of Gd the gadolinides were in closer proximity and contained a higher area percent of gadolinides than the C plane. Therefore, the Charpy impact properties in the T-L orientation and the ductility in the transverse orientation were inferior to the Charpy impact properties in the L-T orientation and the ductility longitudinal to the rolling direction at a given Gd concentration.

Finally, the behavior of the alloy with 230 ppm B and 1.94 wt% Gd was explained when one compared this alloy to the alloy with just 1.90 wt% Gd. It was seen in Figures 20 and 21 that the area percent of gadolinides was smaller and the mean free path was larger for the B containing alloy. So, the quantitative analysis agreed with the observation that the gadolinides were farther apart for both rolling procedures and planes. However, Figure 22 illustrated that generally the average aspect ratio of the gadolinides was larger for the alloy with B. Even the aspect ratio histograms in Figures 29 and 30 comparing the two alloys in each plane for each rolling procedure do not provide much help in explaining the slight increase in elongation and impact energy because they are approximately the same. Therefore, this may be the main reason why the elongation and impact energy were only slightly higher when compared to the alloy with the same concentration of Gd.

5.5 Impact properties and ductility versus V_fR_{EC} and $V_fR_{EC}AR$ parameter

It has already been shown that the mean free path between gadolinides depends on the area fraction of the gadolinides and the particle size (mean R_{EC}). Therefore, the combination of these factors into one parameter, V_fR_{EC}, has been investigated against the impact energy of Ni-Gd-Mo-Cr alloys. Both of these characteristics were chosen because they are linked to the mean free path between the gadolinides. The impact energy was expected to drop as V_fR_{EC} increases because increasing the area fraction of the gadolinides creates more initiation sites for cracks and increasing the size of the gadolinides raises their susceptibility of cracking. In addition, the higher the area fraction of gadolinides leads to an easier coalescence of microcracks because the gadolinides are closer together. It has been shown in previous work with borated stainless steels with chromium borides that the longitudinal impact energy was characterized well by a logarithmic equation with the parameter V_fR_{EC} [11]. Figure 31 shows the longitudinal impact energy data from the borated stainless steel next to the longitudinal and transverse impact energy data from this study. The fit for the borated stainless steels ($R^2 = 0.9744$) was better than the data from the Ni-Gd-Mo-Cr alloys ($R^2 = 0.8931$ for longitudinal data and $R^2 = 0.9658$ for the transverse data), but the Ni-Gd-Mo-Cr alloys were still represented well by the logarithmic equation. Combining both the longitudinal and transverse data established a nice fit ($R^2 = 0.8905$) even though the R^2 value became smaller. It follows in Figure 31 that the ingot impact energy was well represented by a power equation with respect to the V_fR_{EC} parameter. Overall, the logarithmic and power

equations for the longitudinal, transverse, and ingot impact energy versus the V_fR_{EC} parameter represented the data well. Therefore, V_fR_{EC} was a good parameter to show the affect of particle area fraction and size on the toughness of the Ni-Gd-Mo-Cr alloys.

In order to complete this analysis the aspect ratio (AR) was also included. This characteristic of the gadolinides, just like the gadolinide size, increases the probability that the gadolinides crack. Therefore, the V_fR_{EC} parameter was combined with the AR giving a new parameter, $V_fR_{EC}AR$, to further investigate all impact properties and ductility. It can be seen in Figure 32 that the impact energy of both the longitudinal and transverse specimen establishes a logarithmic equation (R^2 = 0.9121) that represents the data slightly better than the V_fR_{EC} parameter. The best-fit power equation for the ingots also increases slightly (R^2 = 0.9277). The $V_fR_{EC}AR$ parameter was plotted against the rest of the impact properties (Figure 33) and ductility quantities (Figure 34) and was shown to represent all these properties well.

5.6 Fracture Toughness of a Ni-Gd-Mo-Cr alloy

The microstructural analysis done on the difference between the gadolinides in the crack propagating planes (T-L orientation) of the cross-rolled and straight-rolled plates also explains why the Ni-Gd-Mo-Cr cross-rolled compact tension specimens typically have higher fracture toughness values than the straight-rolled compact tension specimens (Table IV). Even though there was a drastic drop in the Charpy impact properties of the Ni-Gd-Mo-Cr alloys, the fracture toughness values

of the compact tension (T-L orientation) Ni-Gd-Mo-Cr specimens with a 1.90 wt% Gd were still comparable to heat treated AISI 4340 steel used in aerospace applications, martensitic precipitation-hardened (PH) stainless steels, and borated stainless steels. Heat-treated AISI 4340 steels have a range of K_{IC} values between 48-85 MPa $m^{1/2}$ and martensitic PH stainless steels have values between 50-120 MPa $m^{1/2}$ [17, 18, 19]. These values are similar to the fracture toughness values in Table IV. Additionally, borated stainless steels, like the austenitic stainless steel mentioned previously in this study, have K_{IC} values between 100-200 MPa $m^{1/2}$ [20]. The B grade of the borated stainless steels is at the lower end of that range and the Ni-Gd-Mo-Cr alloys are comparable to those steels. Therefore, the fracture toughness values of the Ni-Gd-Mo-Cr alloys infer that these materials are tougher than one may assume from the Charpy impact energy.

6. Conclusion

The main objective of this research was to determine the effect of Gd concentration on the microstructure and properties of Ni-Gd-Mo-Cr alloys. From this the following conclusions were made:

1. The fracture process of this alloy initiated with the cracking of the gadolinides, microcrack formation, the coalescence of these microcracks, and terminates with fracture.
2. The ingots and hot-rolled plates generally exhibited that the ductility and impact properties of the alloy were inversely proportional to the concentration of Gd.
3. The quantitative analysis of the gadolinide characteristics showed that as the area percent of gadolinides in the crack propagating plane increased, the mean free path between gadolinides became smaller, and as the aspect ratio of the gadolinides increased that the ductility and impact properties decreased.
4. The longitudinal SR plate impact properties and ductility values were always greater than the SR plate transverse impact properties and ductility.
5. The longitudinal and transverse CR plate impact properties and ductility were approximately equal and in between the SR plates.
6. The ingot mechanical properties were the worst out of all the Ni-Gd-Mo-Cr alloys tested.

7. The B containing alloy with 230 ppm slightly increased the impact energy and elongation compared to the alloy with the same concentration of Gd. As the concentration of B increased to 510 ppm the impact energy and elongation were adversely affected.
8. The UTS and yield strength of the Ni-Gd-Mo-Cr alloys generally increased slightly as the Gd concentration rose.
9. The Ni-Gd-Mo-Cr plate microstructures may be classified between spheres with a constant radius in a matrix and randomly oriented rods in a matrix.
10. The logarithmic and power equations for the longitudinal, transverse, and ingot impact properties and ductility versus the $V_f R_{EC} AR$ parameter represent the data well.
11. The fracture toughness values of the Ni-Gd-Mo-Cr alloys inferred that these alloys are tougher than the Charpy impact energies display.

Table I: Ni-Gd-Mo-Cr alloy compositions

	Element (wt%)										
Alloy	Ni	Mo	Cr	Fe	Gd	P	S	Si	O	N	C	B
1	67.8	15.9	16.1	0.088	0.00	<0.001	<0.001	0.088	0.0024	0.0040	0.0065	-
2	67.7	15.7	16.0	0.016	0.460	<0.001	<0.001	0.070	0.0044	0.0045	0.0052	-
3	67.2	15.5	16.1	0.017	1.01	<0.001	<0.001	0.081	<0.001	0.0044	<0.005	-
4	66.9	15.6	15.9	0.015	1.49	<0.001	<0.001	0.070	<0.001	0.0039	0.0064	-
5	66.8	15.2	16.0	0.016	1.90	<0.001	<0.001	0.070	0.0021	0.0041	0.0065	-
6	66.7	15.1	15.6	0.016	2.45	<0.001	<0.001	0.071	0.0056	0.0043	0.0066	-
7	66.9	14.8	16.2	0.037	1.94	<0.001	<0.001	0.009	0.0021	0.0045	0.0086	0.023
9	67.4	14.6	15.8	0.030	2.02	<0.005	<0.005	0.030	<0.005	0.0020	0.0135	0.051

Table II: Composition of the Ni-Gd-Mo-Cr alloy for tensile testing to understand the fracture process of a brittle phase in a ductile matrix

Alloy M323	
Element	wt%
Al	0.05
B	0.0015
C	0.009
Co	0.01
Cr	15.84
Cu	0.04
Fe	0.01
Gd	2.41
Hf	0.004
Mg	52
Mn	0.01
Mo	15.28
N	23 ppm
Nb	0.007
Ni	bal
O	3 ppm
P	0.001
S	0.0002
Si	0.001
Ta	0.004
Ti	0.004
V	0.003
W	0.04
Zr	0.008

Table III: Composition of the Ni-Gd-Mo-Cr alloy for fracture toughness testing

Alloy M339	
Element	wt%
C	0.0064
Co	0.001
Cr	15.71
Fe	0.006
Gd	1.9
Mg	0.003
Mn	<0.001
Mo	14.50
N	<0.001
Ni	Balance
O	0.0038
P	<0.005
S	<0.001
Si	<0.005

Table IV: $J_{(IC)}$ and corresponding $K(J_{IC})$ of CR and SR plates in T-L orientation

Test ID	E Msi	J_{IC} (in-lb/in2)	$K(J_{IC})$ (ksi $\sqrt{in}$)	$K(J_{IC})$ (MPa$\sqrt{m}$)
CR				
Trial 1	32.0	210	84.2	92.5
Trial 2	31.9	221	86.4	94.9
SR				
Trial 1	31.7	173	76.4	84.0
Trial 2	31.8	193	80.8	88.8

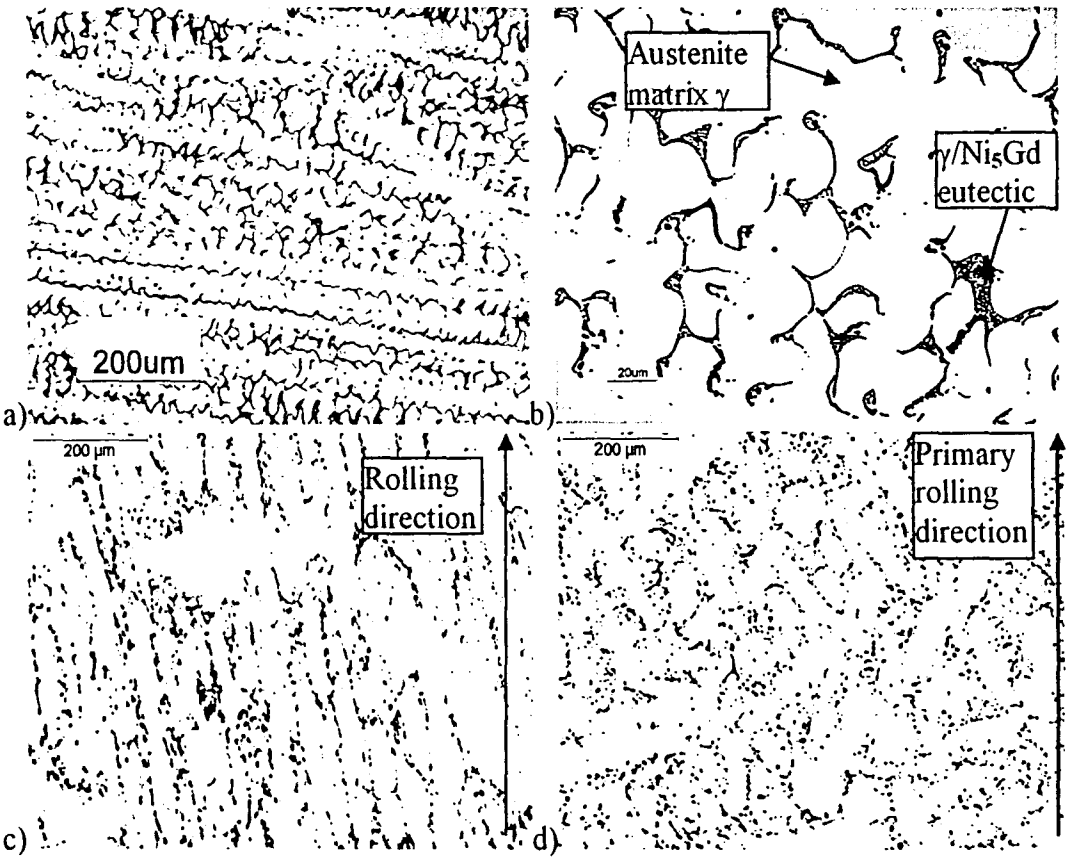

Figure 1: a&b) Ingot microstructure of a Ni-Gd-Mo-Cr alloy with 1.90 wt% Gd (#5 in Table I) c) Straight-rolled microstructure counterpart of alloy with 1.90 wt% Gd (top of the plate view) d) Cross-rolled microstructure counterpart of alloy with 1.90 wt% Gd (top of the plate view)

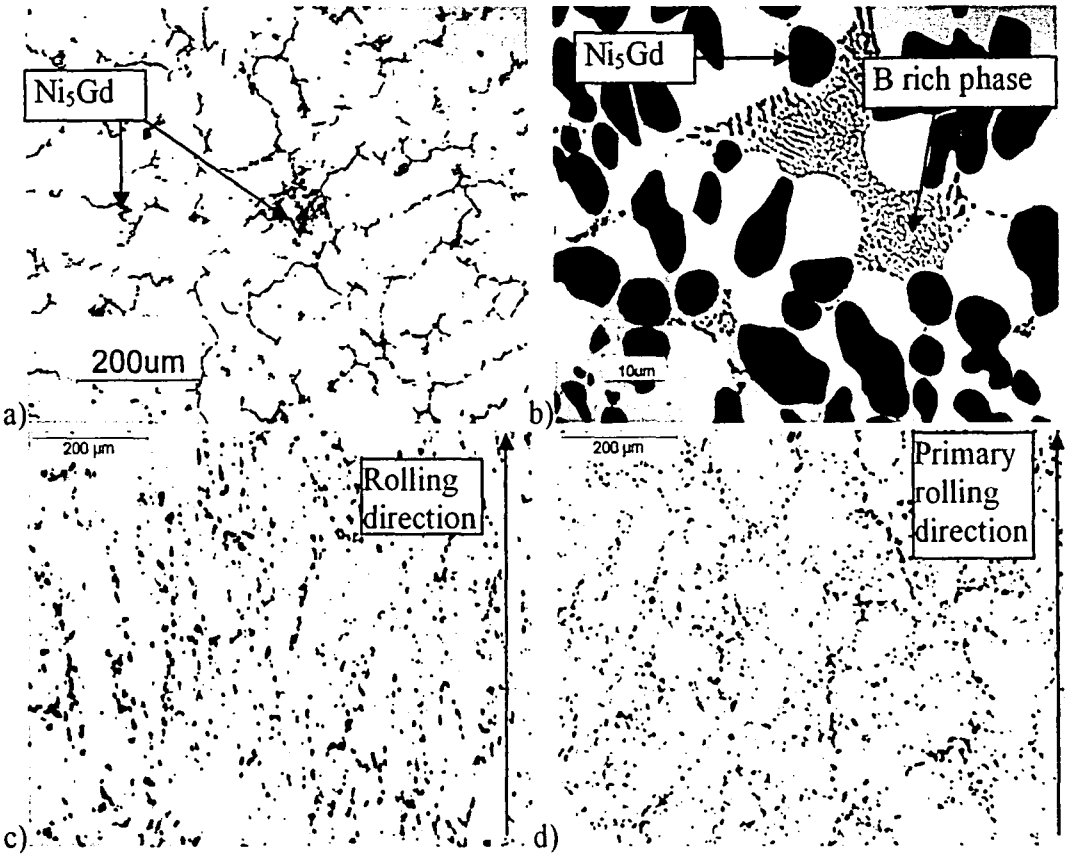

Figure 2: a&b) Ingot microstructure of a Ni-Gd-Mo-Cr alloy with 1.94 wt% Gd and 230 ppm of B(#7 in Table I) c) Straight-rolled microstructure counterpart of alloy in (a) and (b) (top of the plate view) d) Cross-rolled microstructure counterpart of alloy in (a) and (b) (top of the plate view)

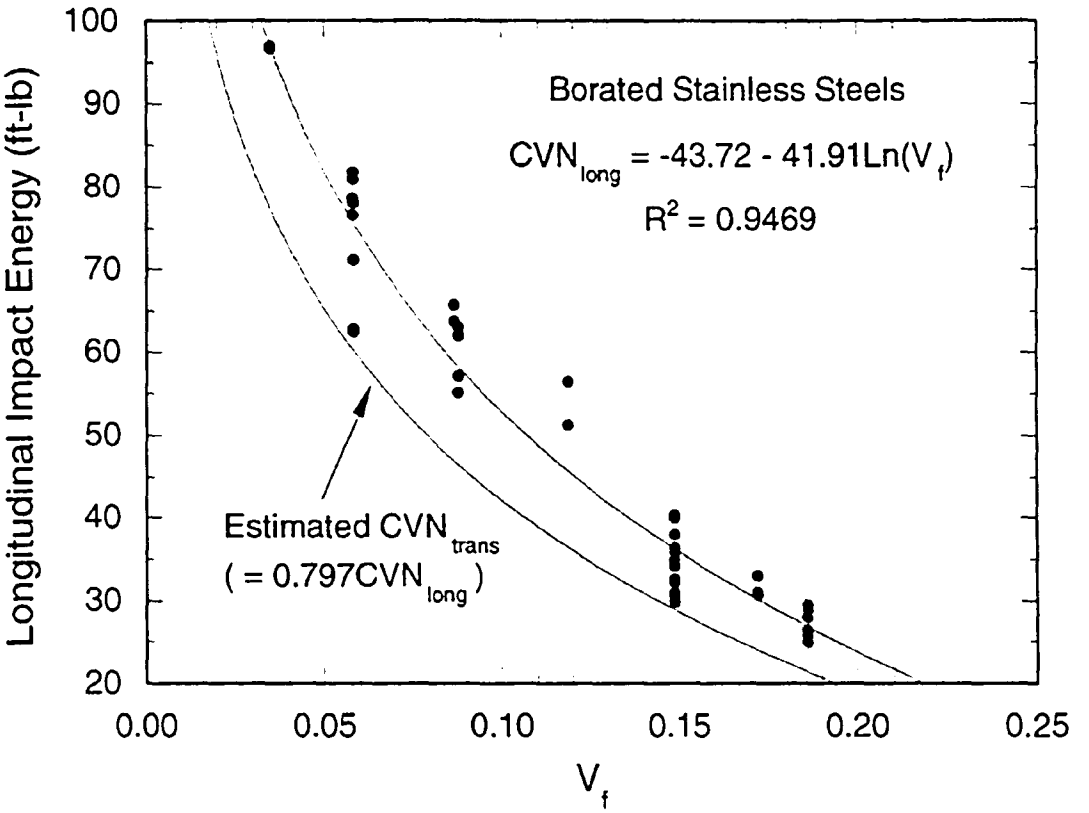

Figure 3: Longitudinal impact energy for borated stainless steels as a function of the volume fraction of chromium borides.

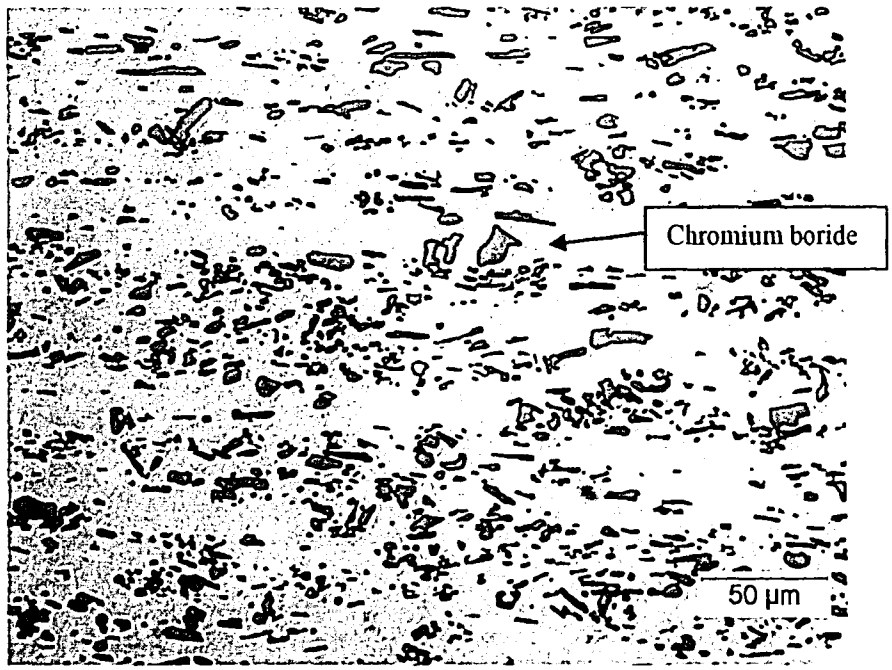

(a)

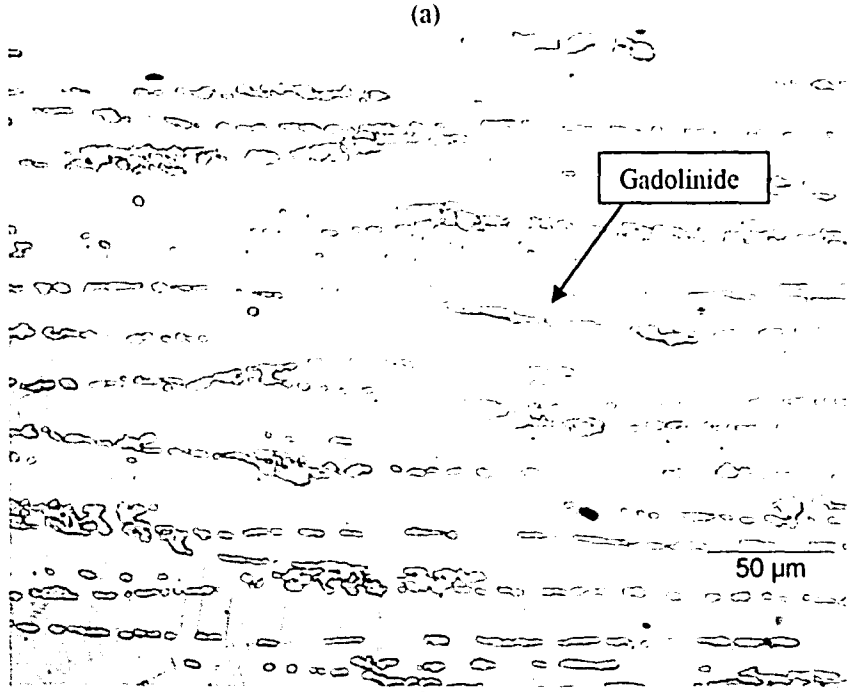

(b)

Figure 4: a) Unaffected microstructure of BSS b) Unaffected microstructure of Ni-Gd-Mo-Cr alloy

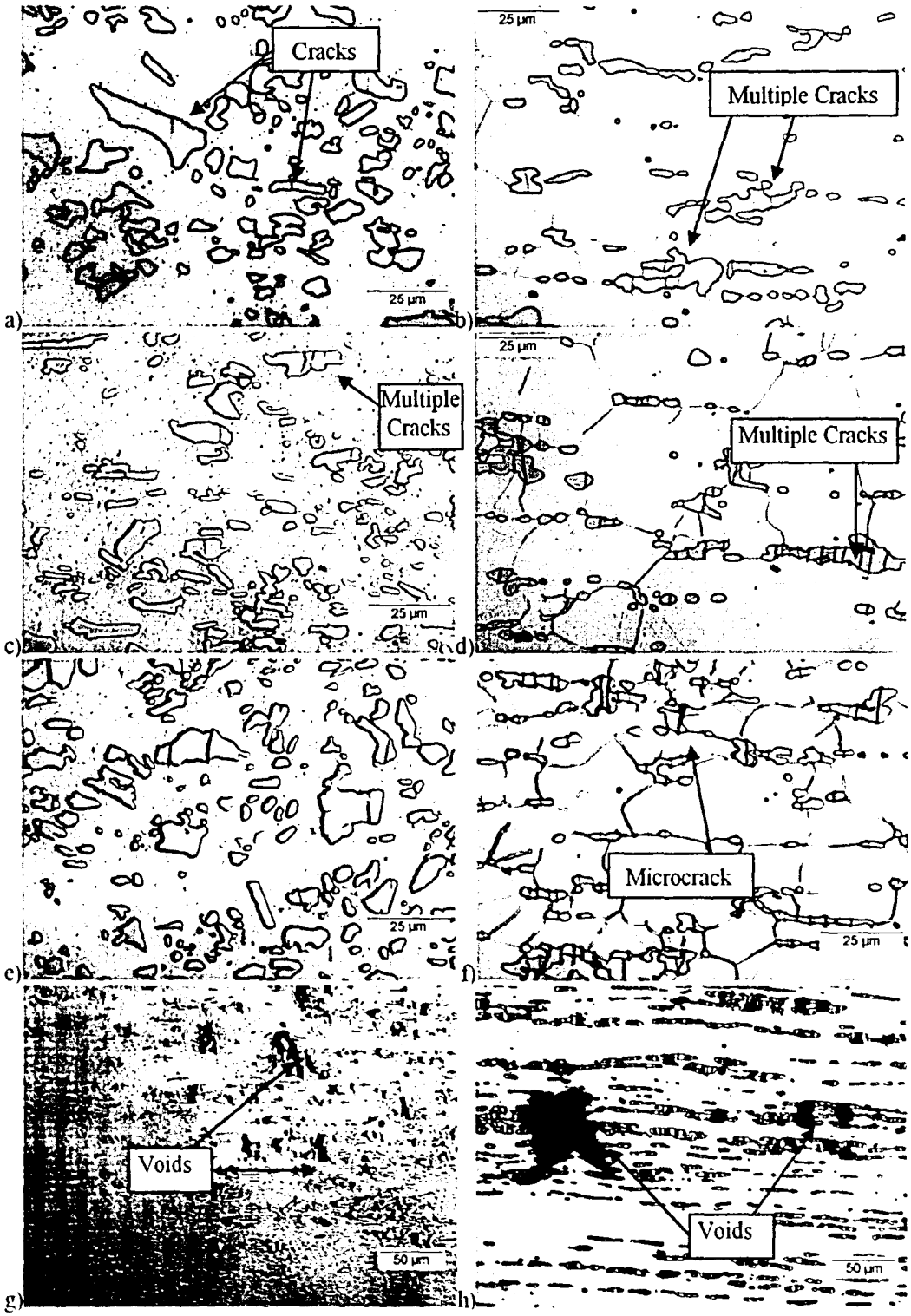

Figure 5: a) 2% strained BSS b) 2% strained Ni-Gd-Mo-Cr c) 4% strained BSS d) 4% strained Ni-Gd-Mo-Cr e) 6% strained BSS f) 6% strained Ni-Gd-Mo-Cr g) Failed BSS sample directly next to fracture surface h) Failed Ni-Gd-Mo-Cr sample directly next to fracture surface in the same area as (g)

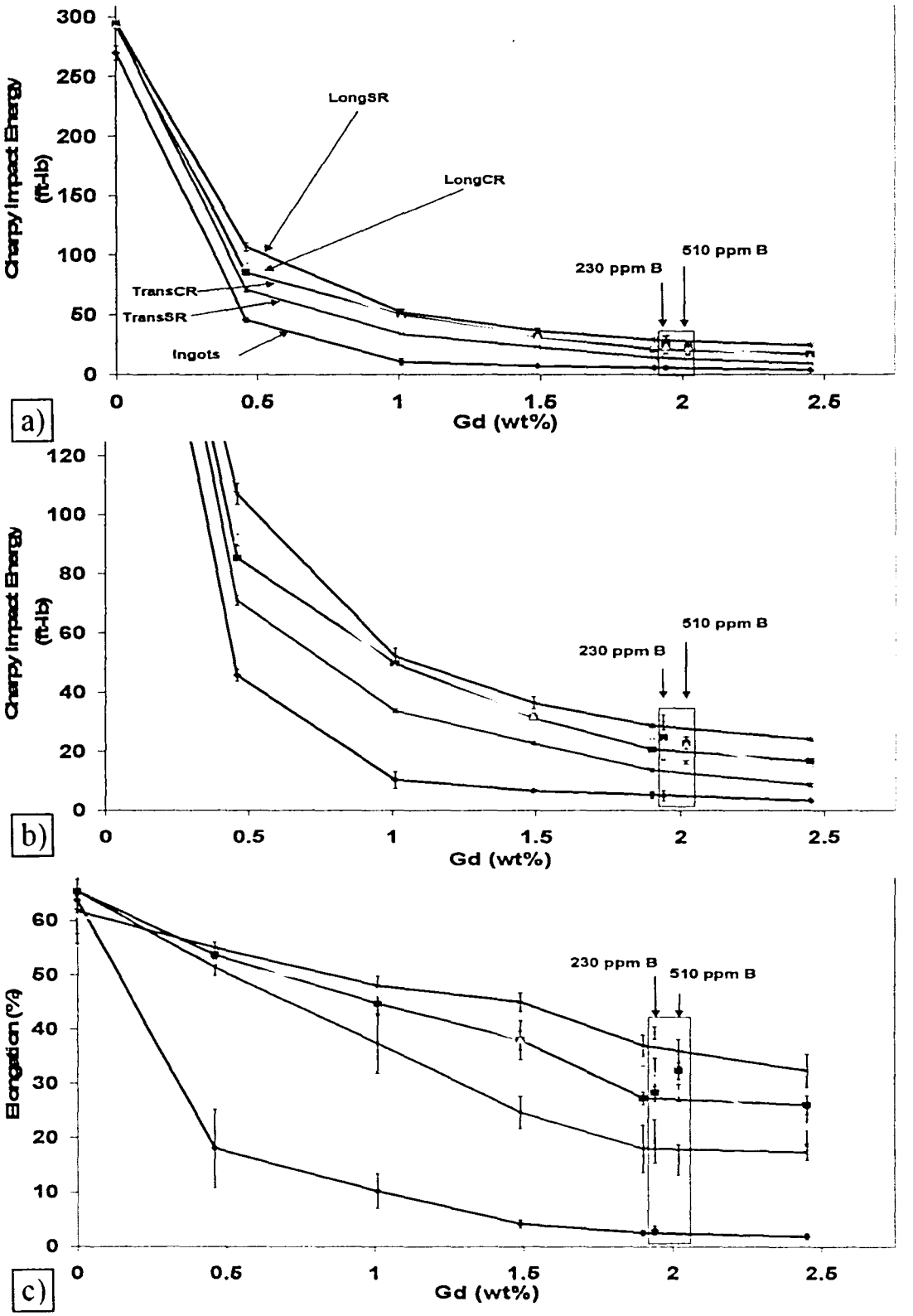

Figure 6: a) Charpy impact energy versus Gd concentration for all Ni-Gd-Mo-Cr ingots and plates b) Zoom in of (a) c) Elongation versus Gd concentration for all Ni-Gd-Mo-Cr ingots and plates

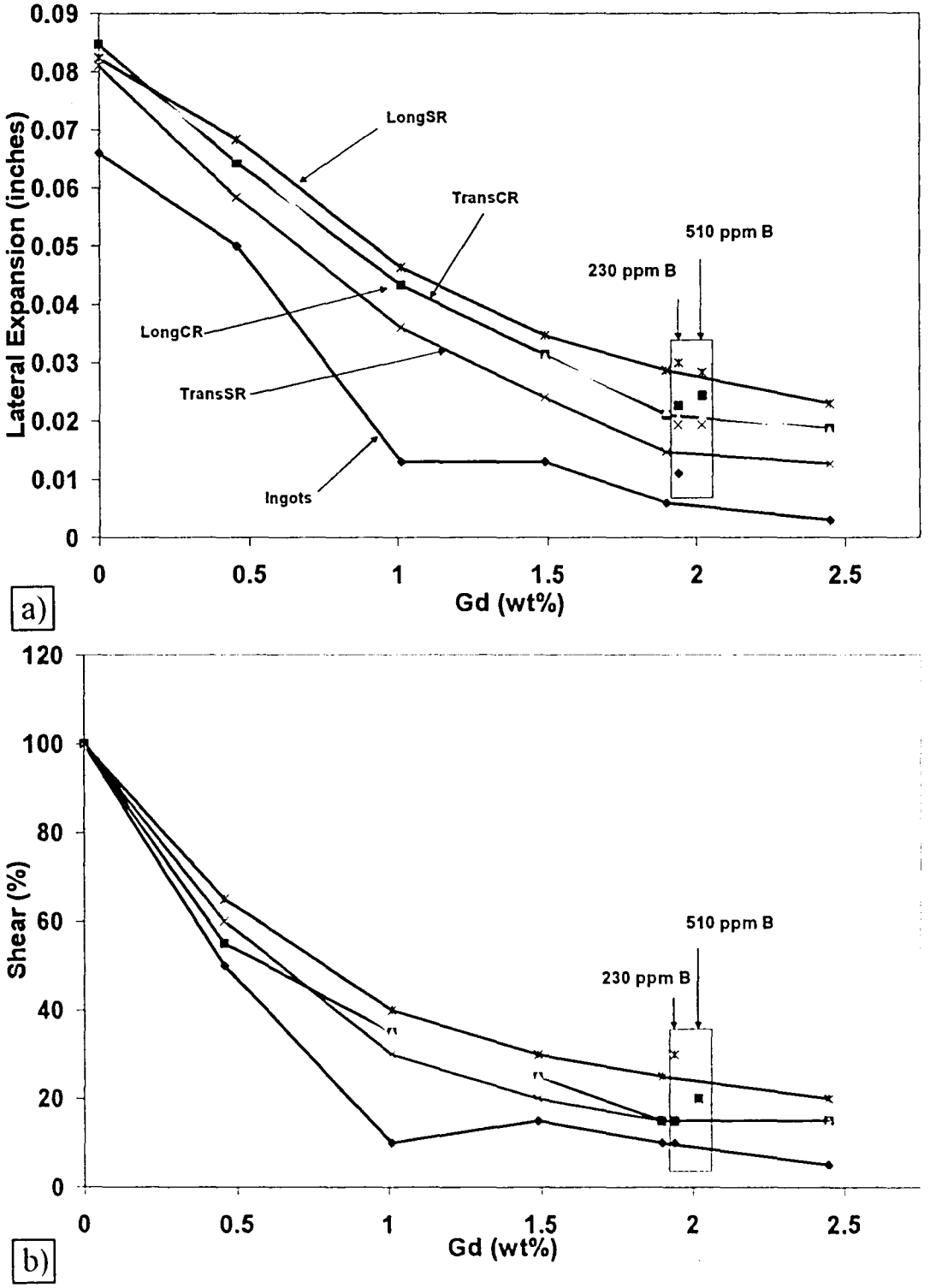

Figure 7: (a) Lateral expansion versus Gd concentration for all Ni-Gd-Mo-Cr ingots and plates (b) Shear percentage versus Gd concentration for all Ni-Gd-Mo-Cr ingots and plates

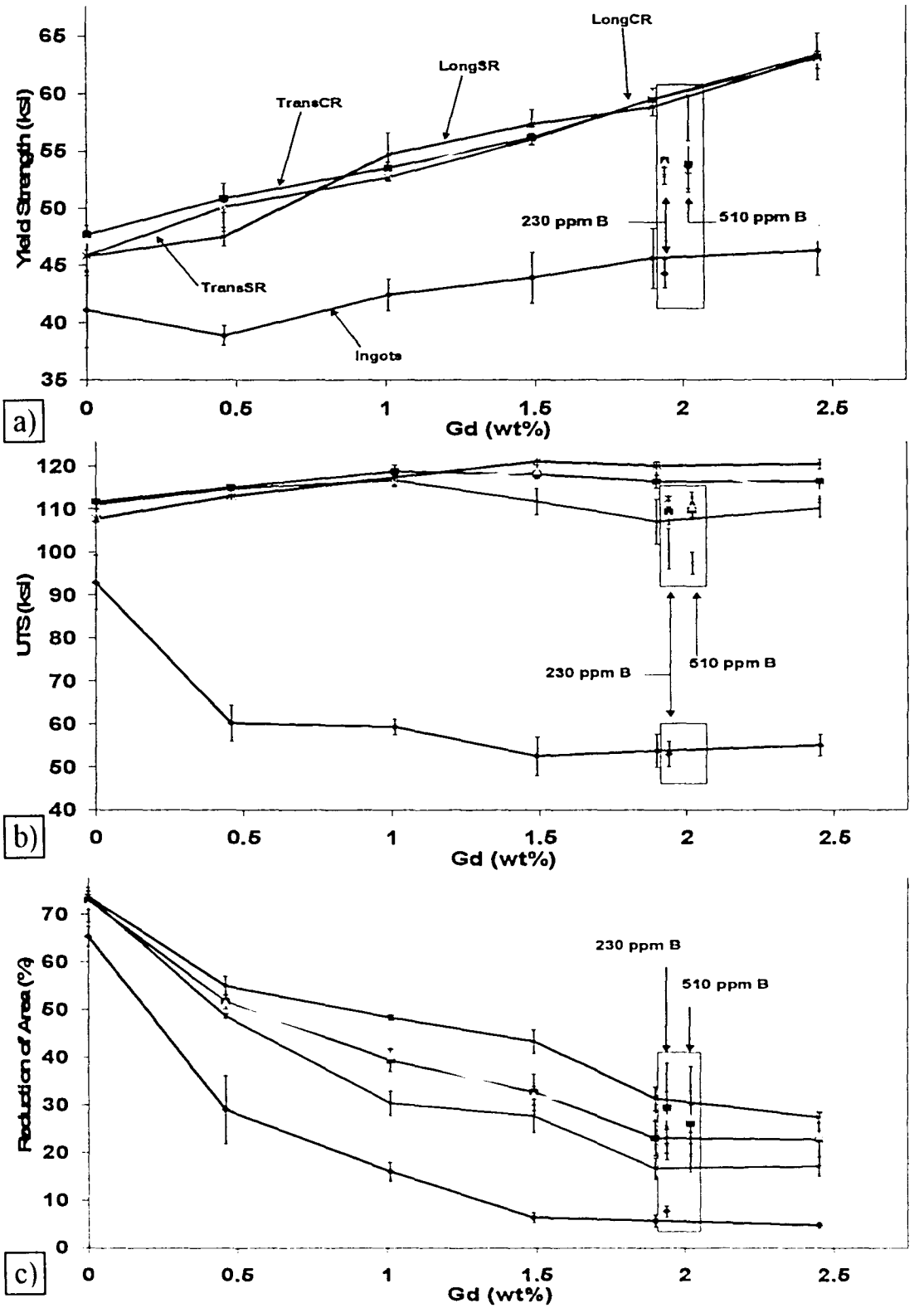

Figure 8: a) Yield strength versus Gd concentration for all Ni-Gd-Mo-Cr ingots and plates b) UTS versus Gd concentration for all Ni-Gd-Mo-Cr ingots and plates c) Reduction of area versus Gd concentration for all Ni-Gd-Mo-Cr ingots and plates

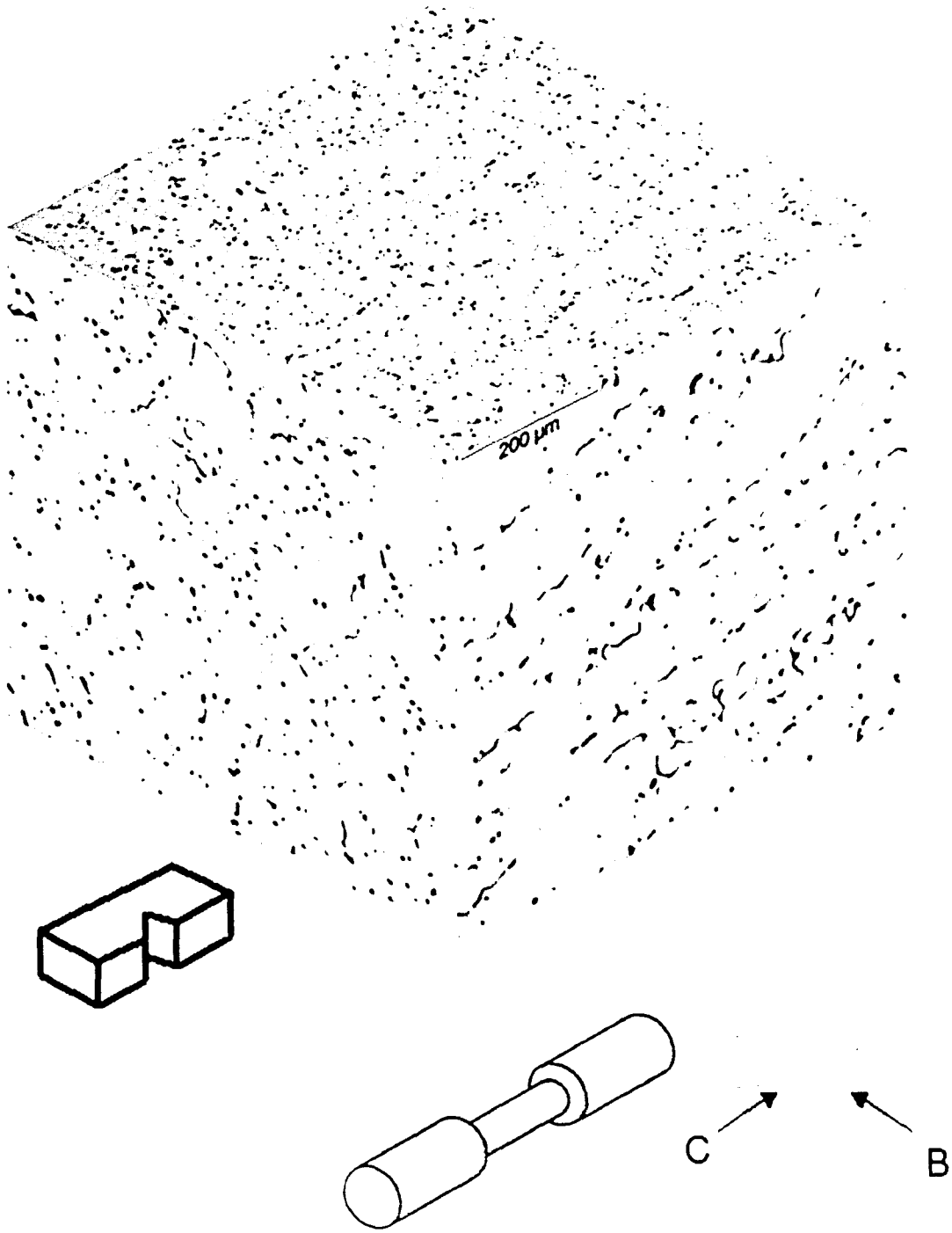

Figure 9: 3D representation of the Ni-Gd-Mo-Cr ingot with 0.46 wt% Gd

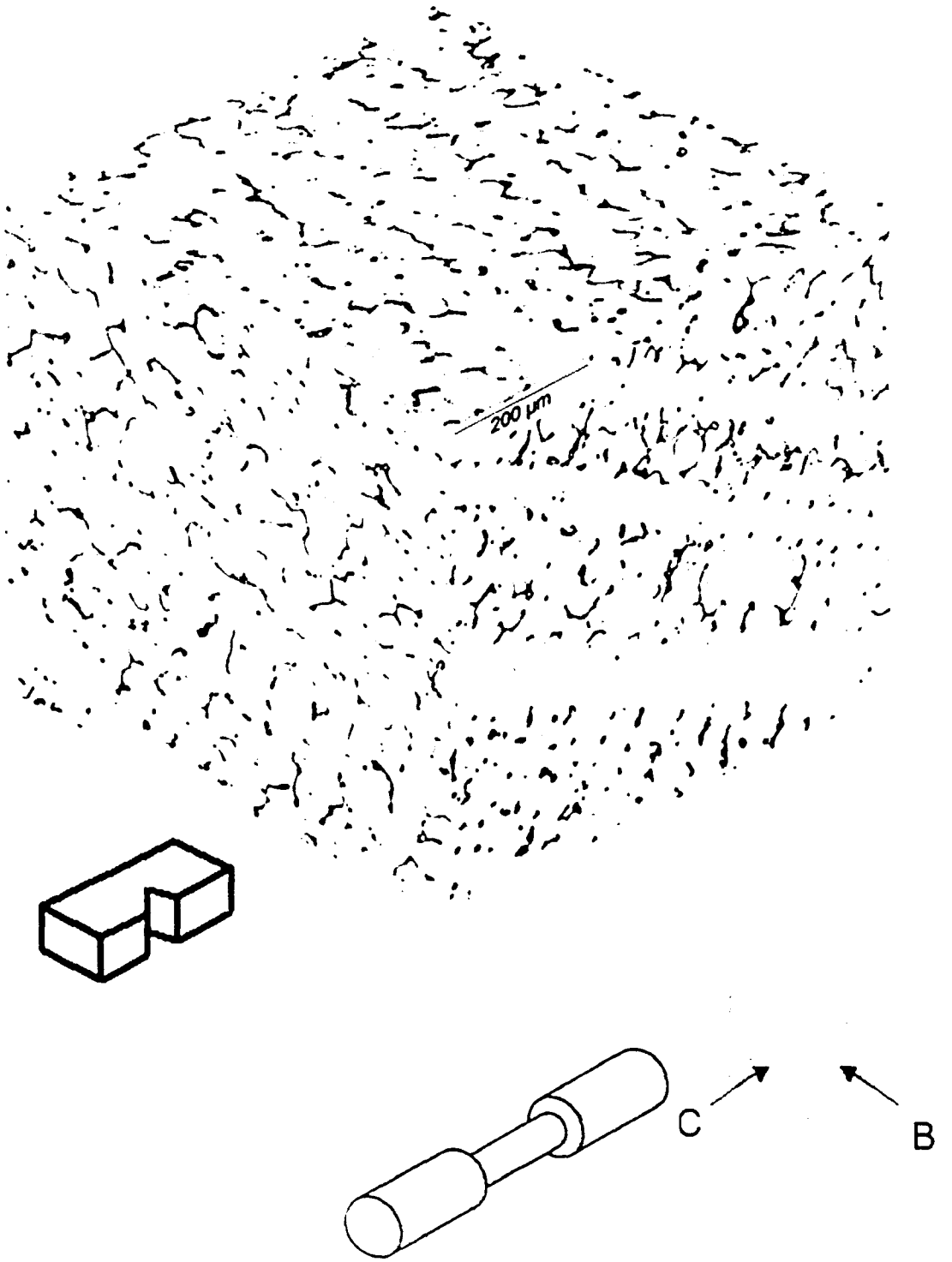

Figure 10: 3D representation of the Ni-Gd-Mo-Cr ingot with 1.01 wt% Gd

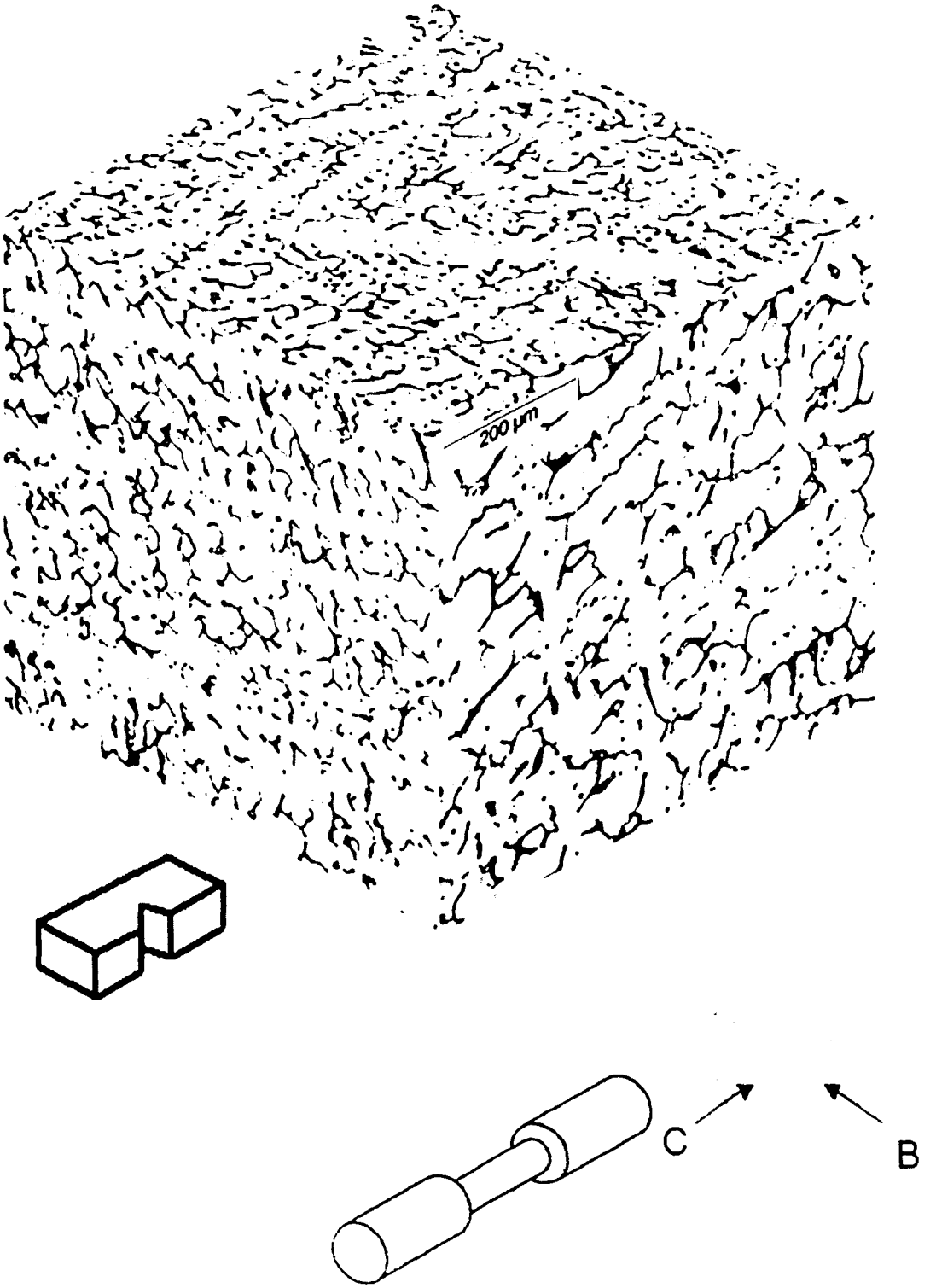

Figure 11: 3D representation of the Ni-Gd-Mo-Cr ingot with 1.90 wt% Gd

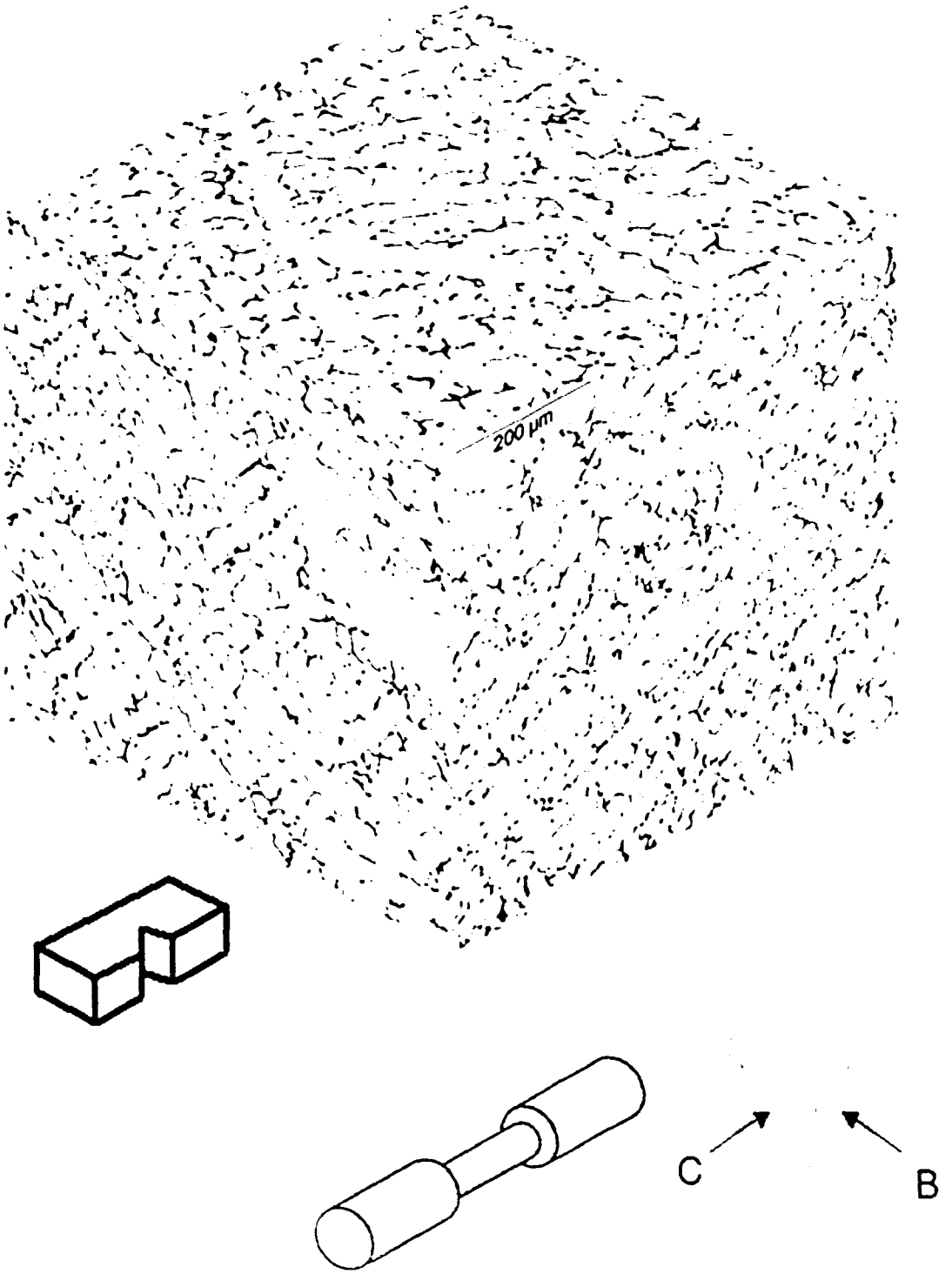

Figure 12: 3D representation of the Ni-Gd-Mo-Cr ingot with 1.94 wt% Gd and 230 ppm B

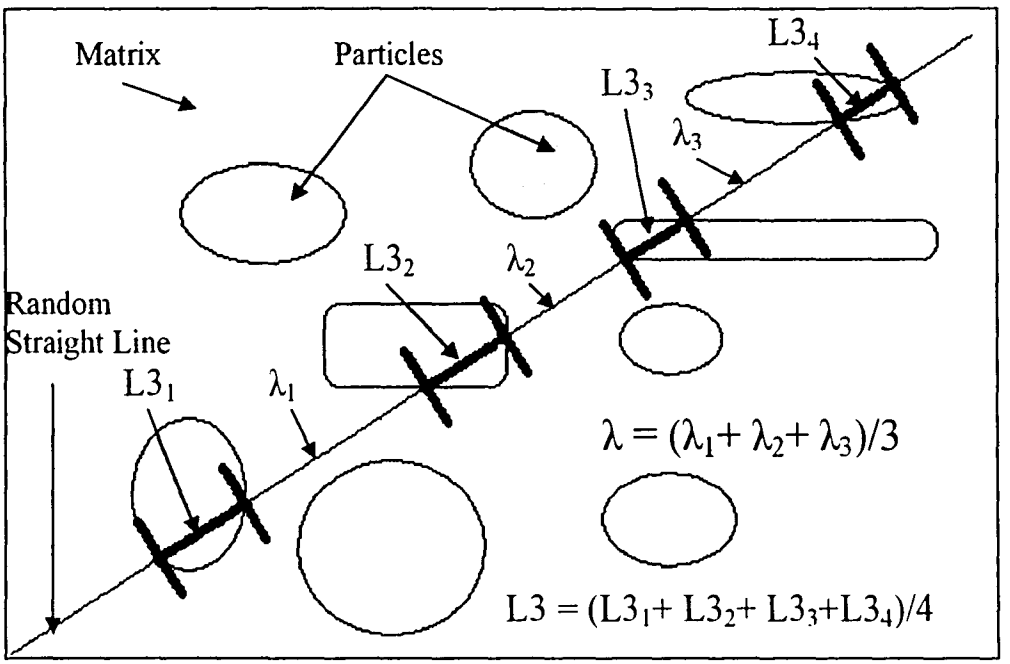

Figure 13: Schematic of mean free path

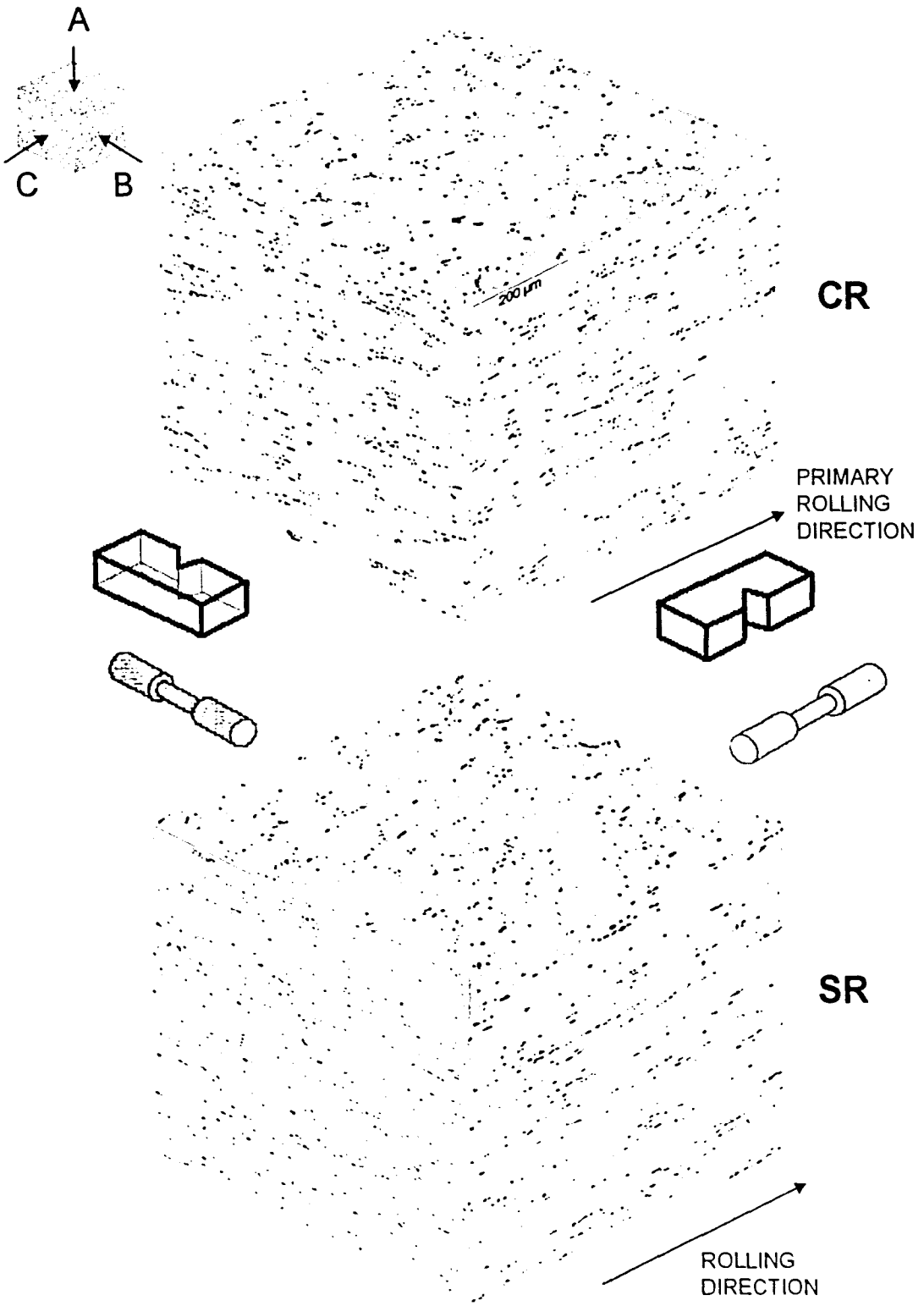

Figure 14: 3D representation of the Ni-Gd-Mo-Cr cross-rolled plate (top) and straight-rolled plate (bottom) with 0.46 wt% Gd

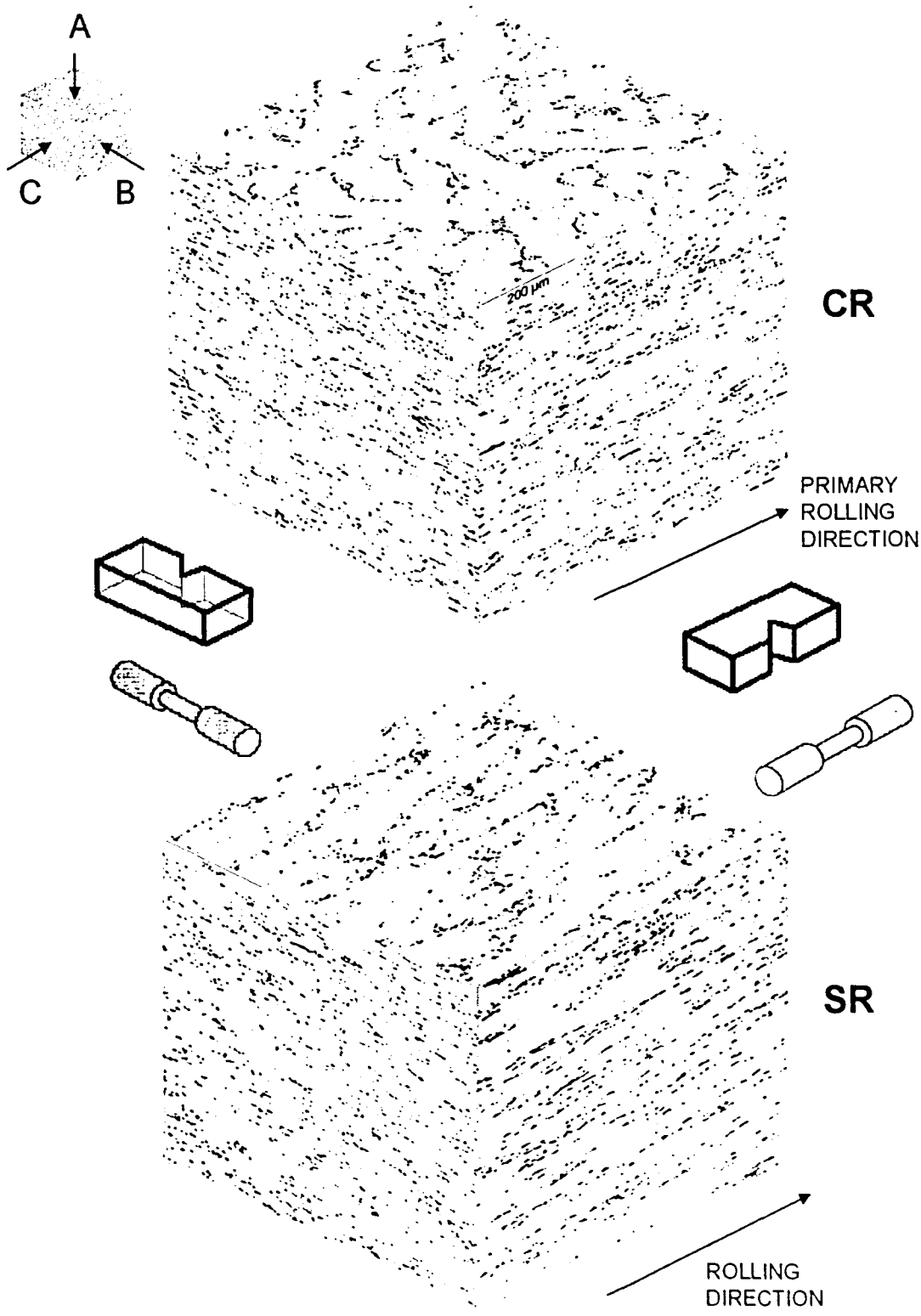

Figure 15: 3D representation of the Ni-Gd-Mo-Cr cross-rolled plate (top) and straight-rolled plate (bottom) with 1.01 wt% Gd

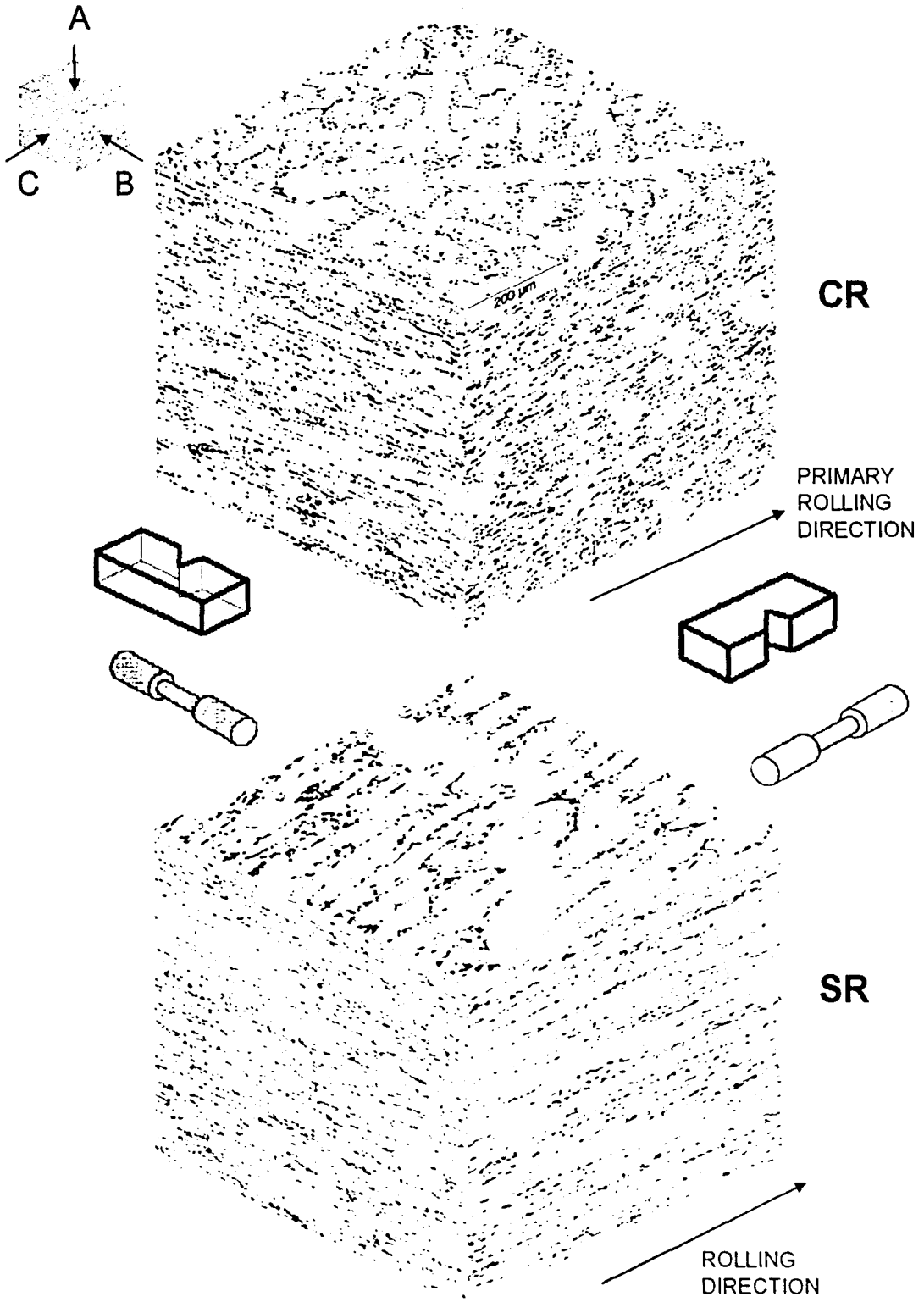

Figure 16: 3D representation of the Ni-Gd-Mo-Cr cross-rolled plate (top) and straight-rolled plate (bottom) with 1.90 wt% Gd

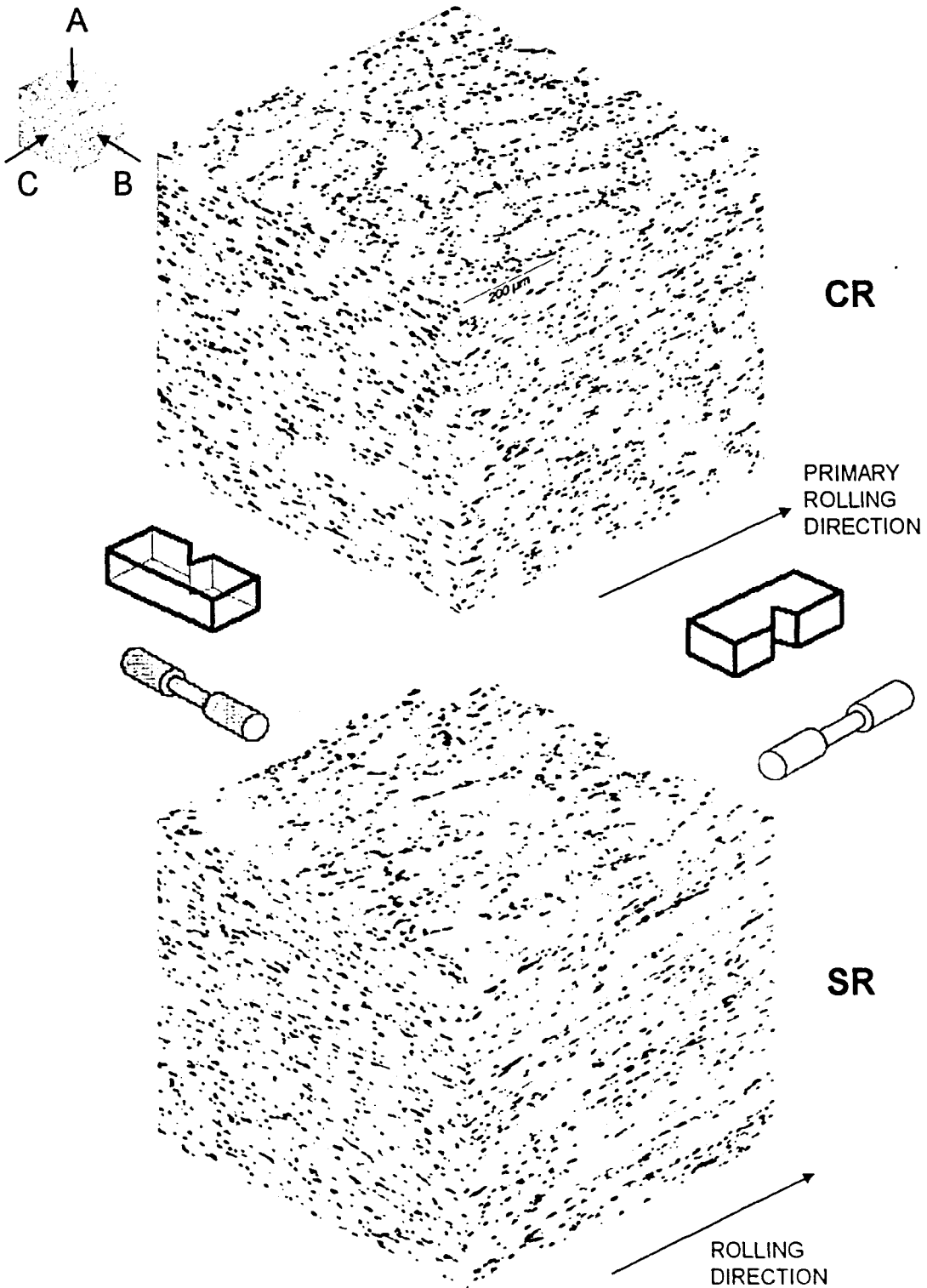

Figure 17: 3D representation of the Ni-Gd-Mo-Cr cross-rolled plate (top) and straight-rolled plate (bottom) with 1.94 wt% Gd and 230 ppm B

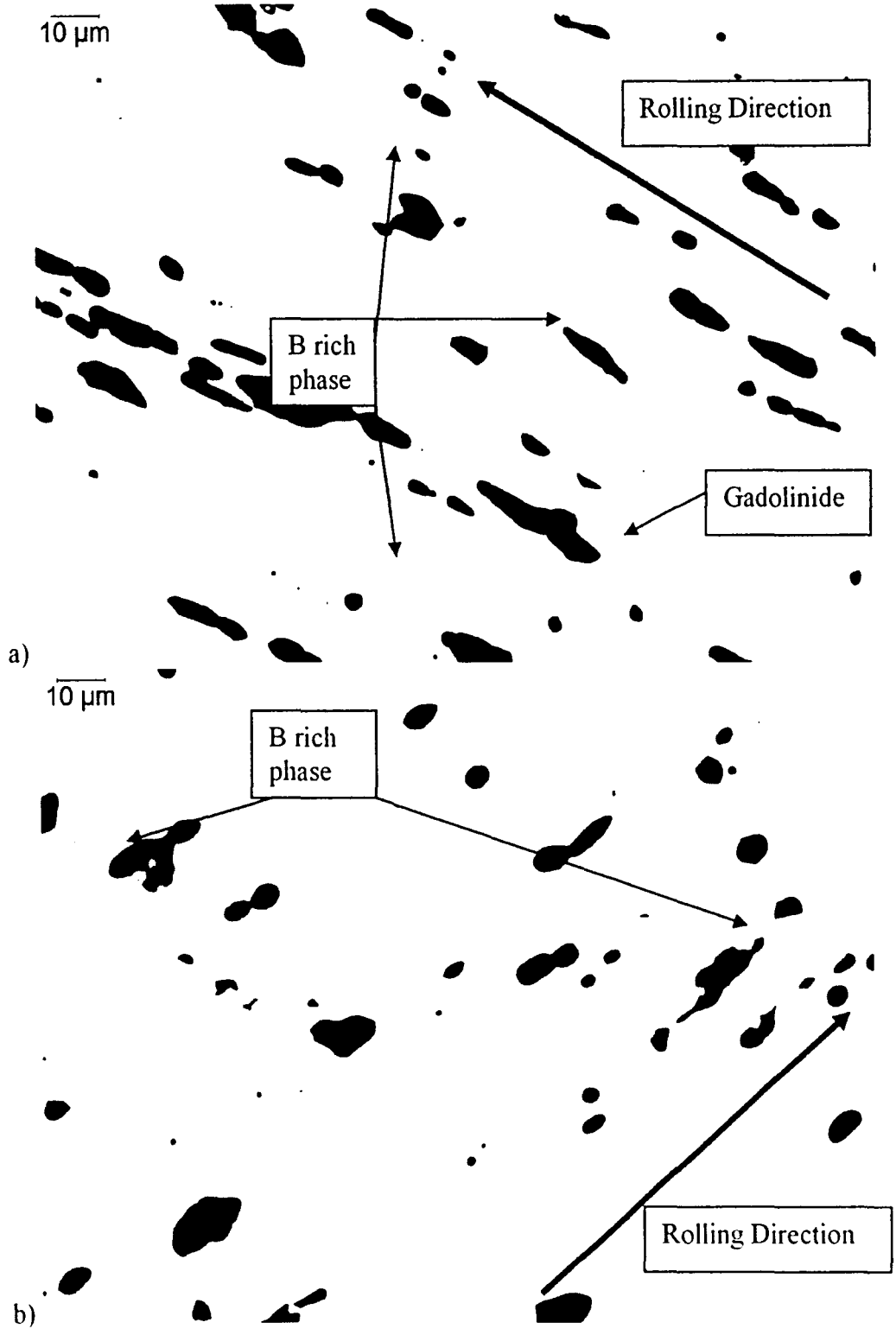

Figure 18: a) Micrograph of SR plate (230ppm) longitudinal to the rolling direction showing B rich phase b) Micrograph of SR plate (510 ppm) longitudinal to the rolling direction showing the B rich phase

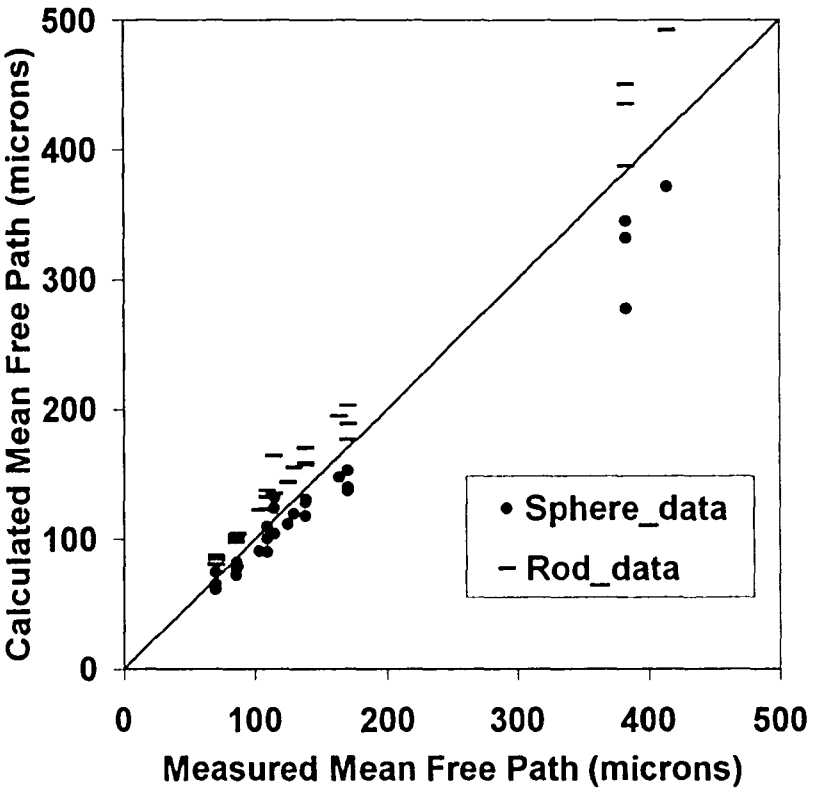

Figure 19: Calculated mean free path versus the measured mean free path for both the B and C planes of the SR and CR plates using the sphere and rod data.

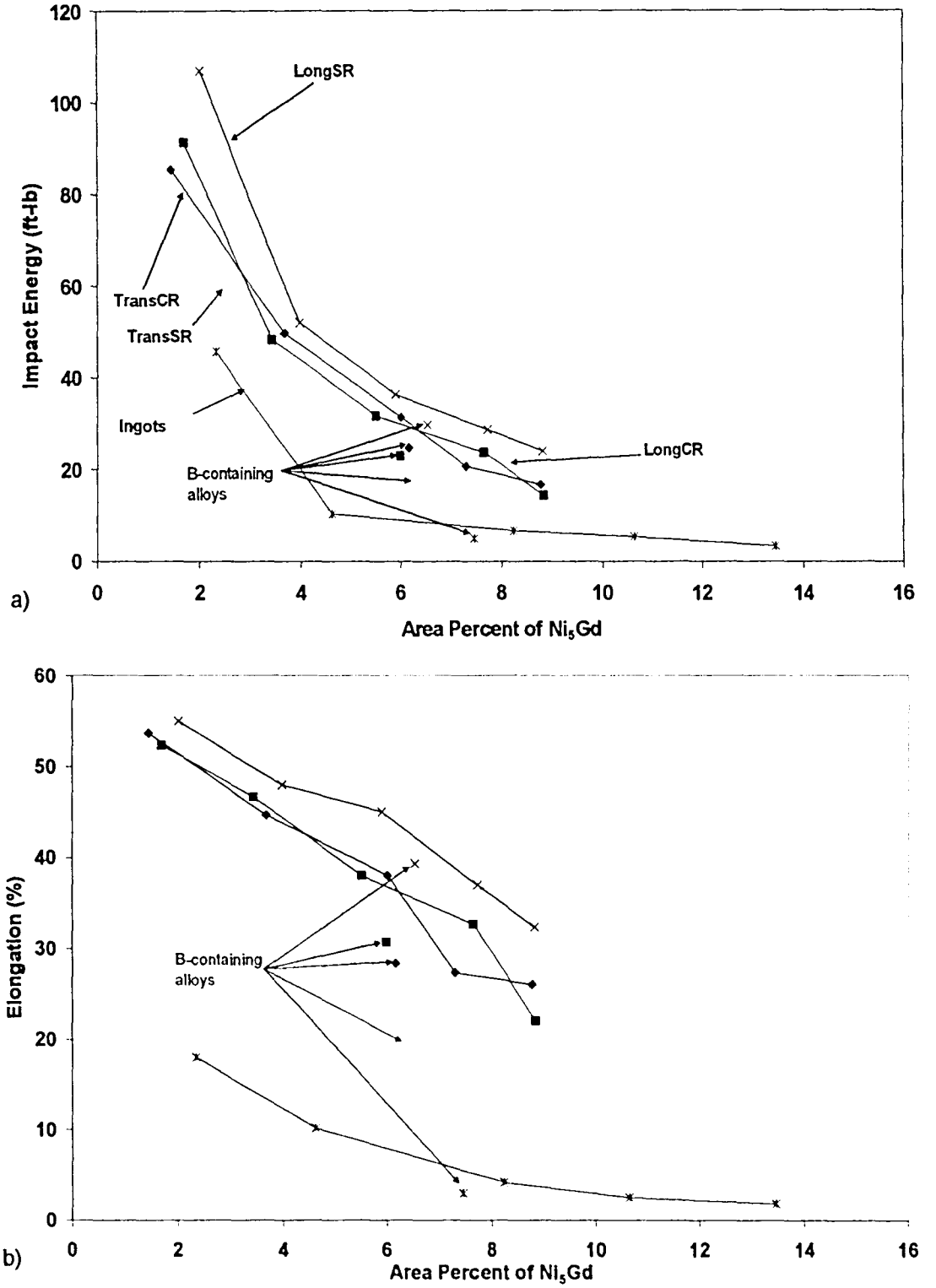

Figure 20: a) Impact energy versus area percent of gadolinides graph b) Elongation versus area percent of gadolinides graph

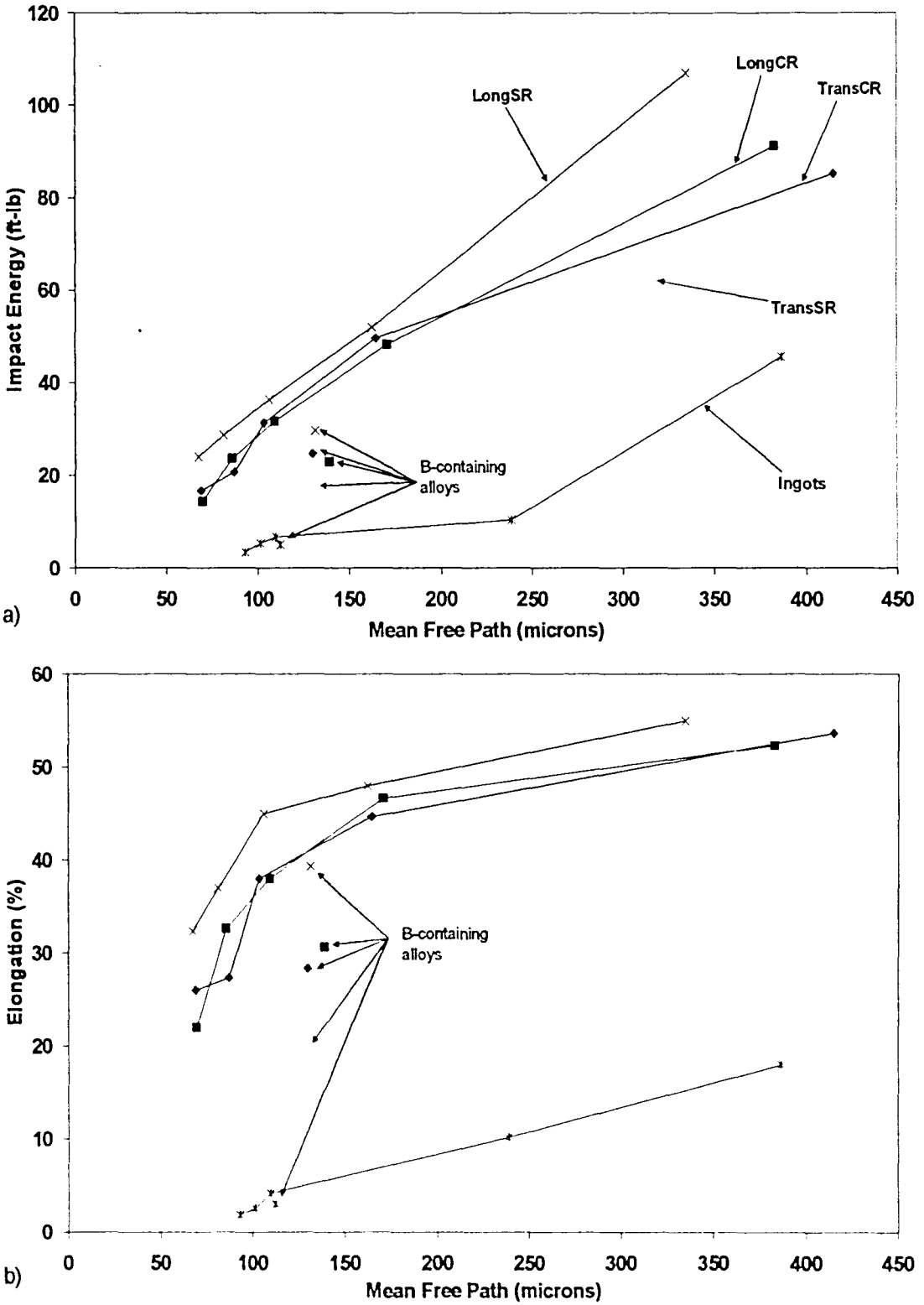

Figure 21: a) Impact energy versus mean free path graph b) Elongation versus mean free path graph

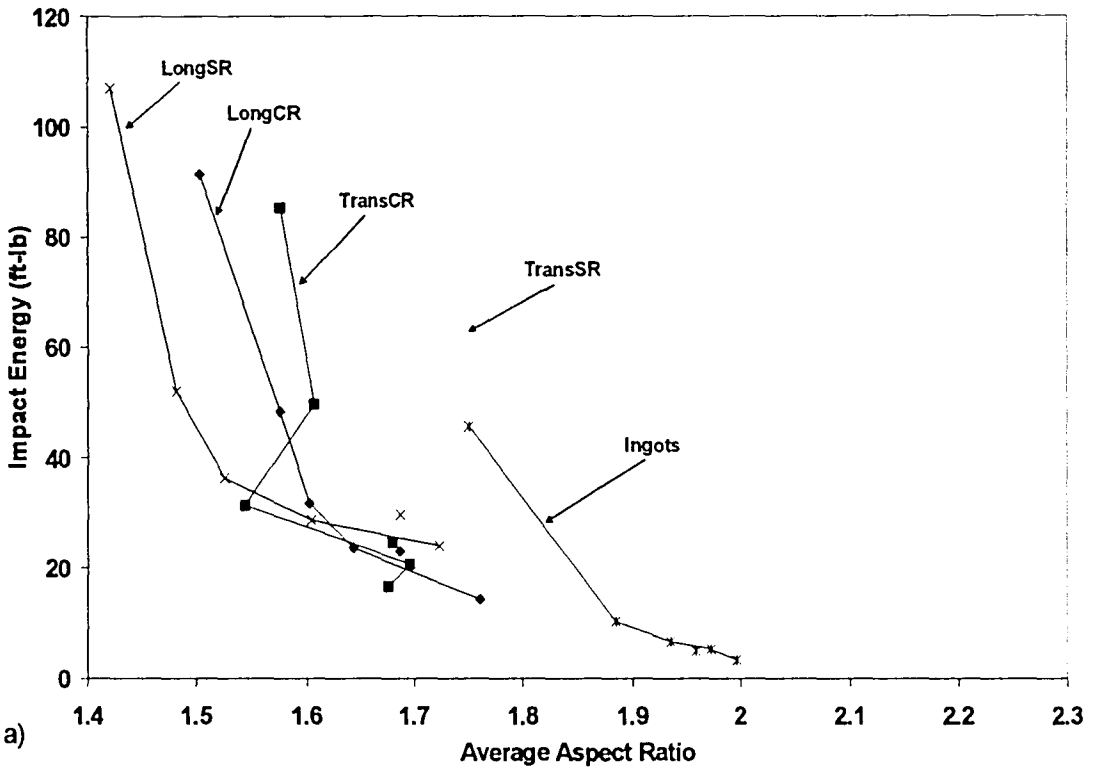

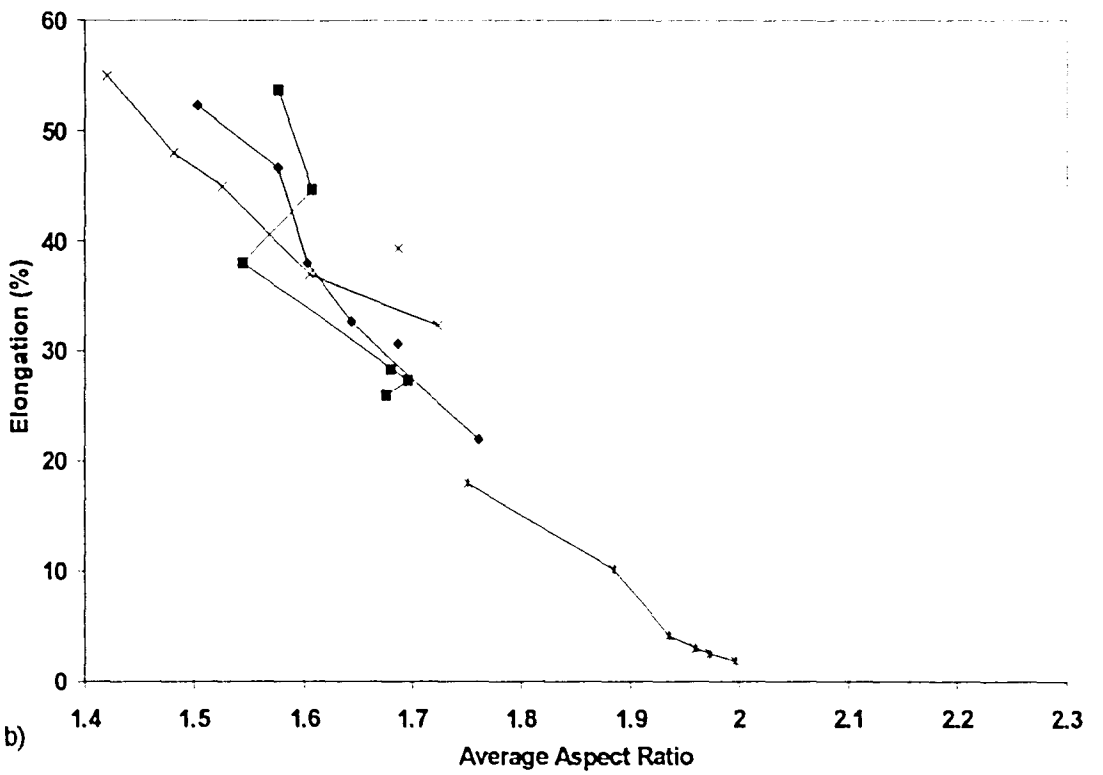

Figure 22: a) Impact energy versus aspect ratio of gadolinides graph b) Elongation versus aspect ratio of gadolinides graph

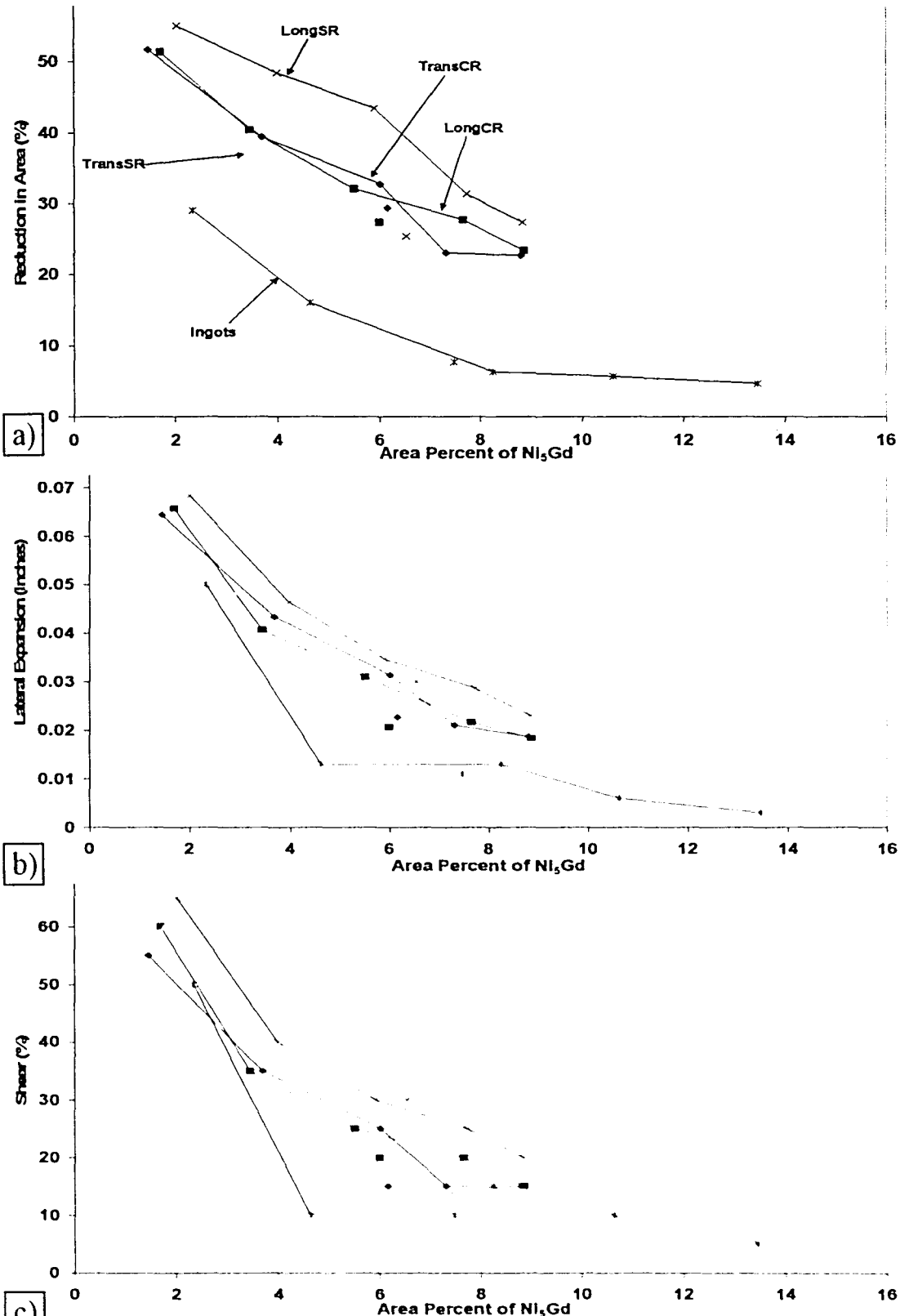

Figure 23: (a) Reduction in area, (b) Lateral Expansion, and (c) Shear percentage versus area percent of gadolinides graphs

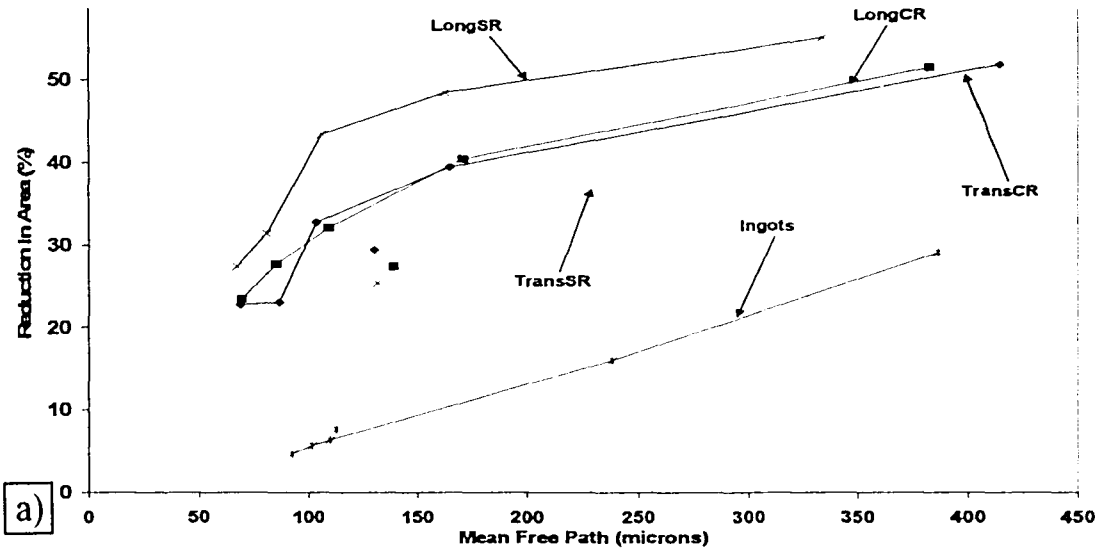

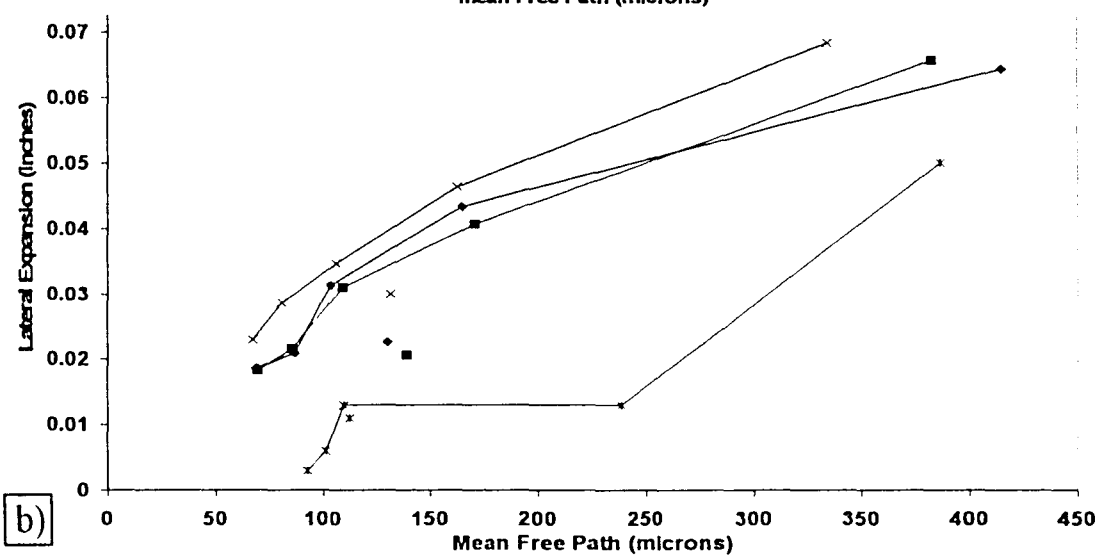

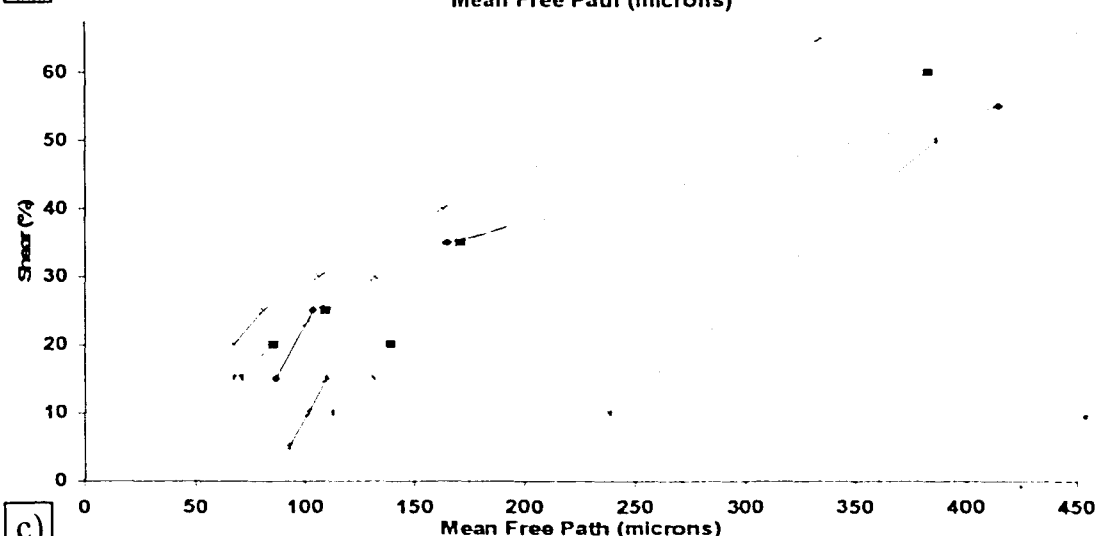

Figure 24: (a) Reduction in area, (b) Lateral Expansion, and (c) Shear percentage versus mean free path of gadolinides graphs

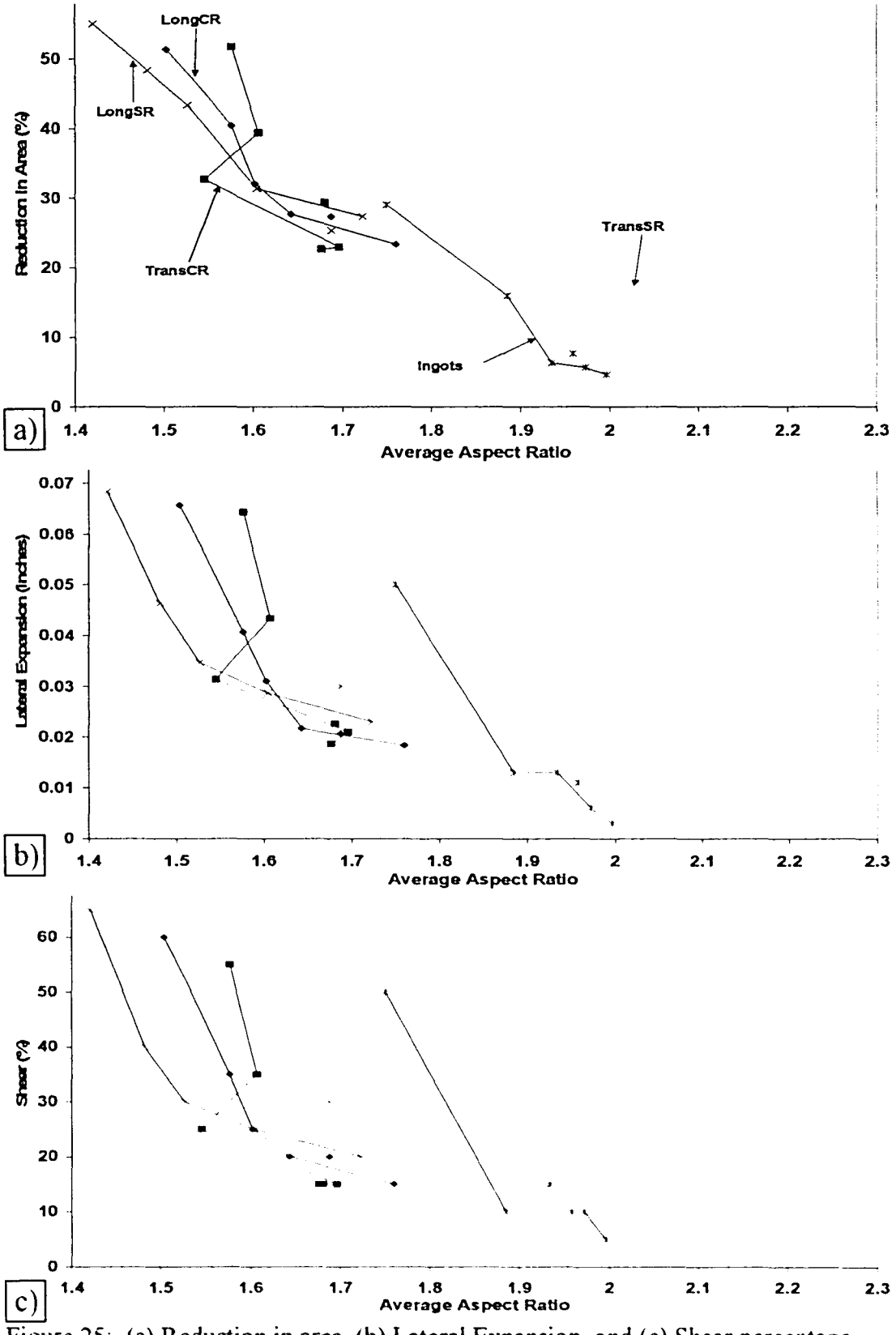

Figure 25: (a) Reduction in area, (b) Lateral Expansion, and (c) Shear percentage versus average aspect ratio of gadolinides graphs

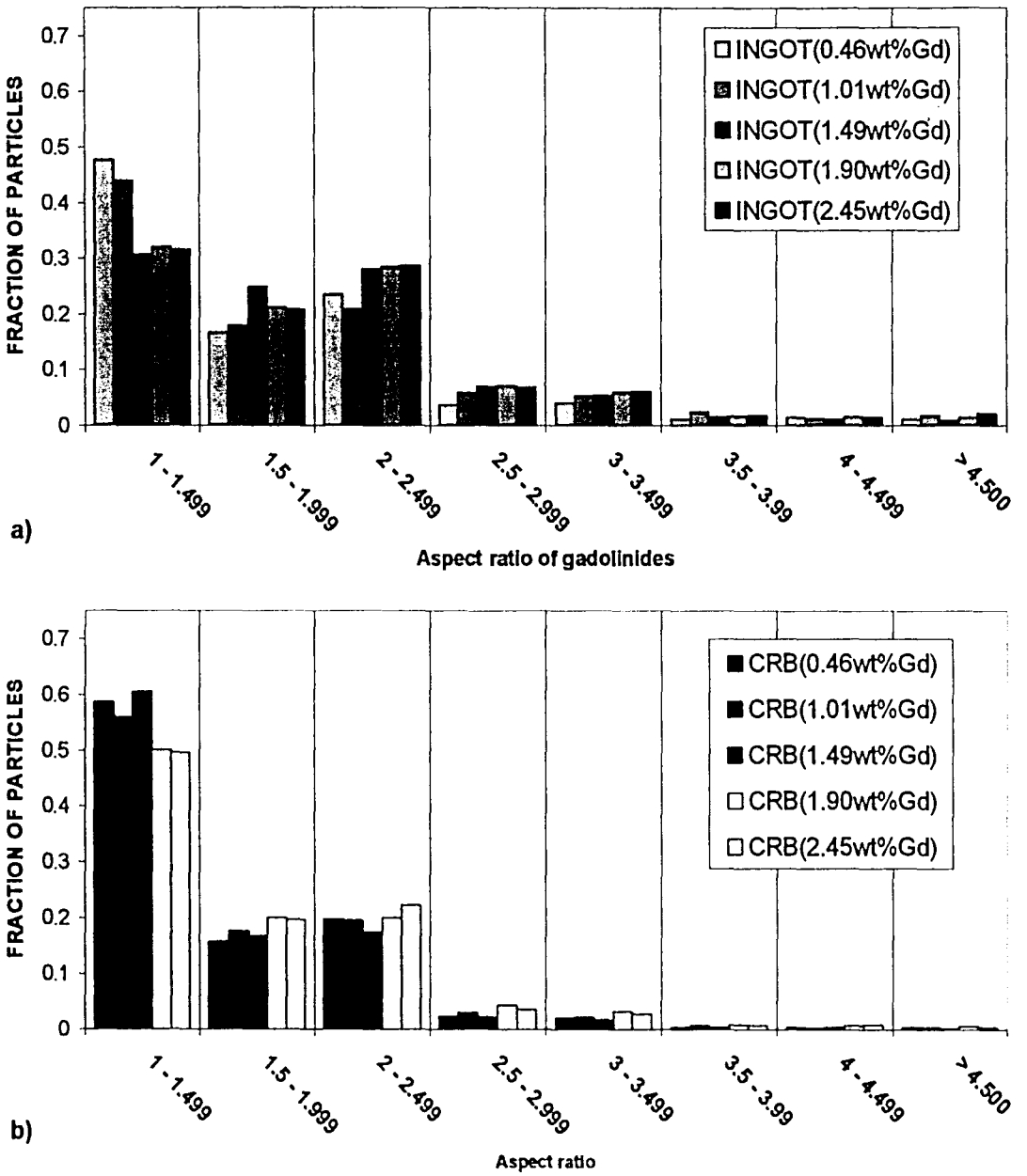

Figure 26: a) Aspect ratio histograms for all ingots except the B containing b) Aspect ratio histograms for the CR plates transverse to the primary rolling direction

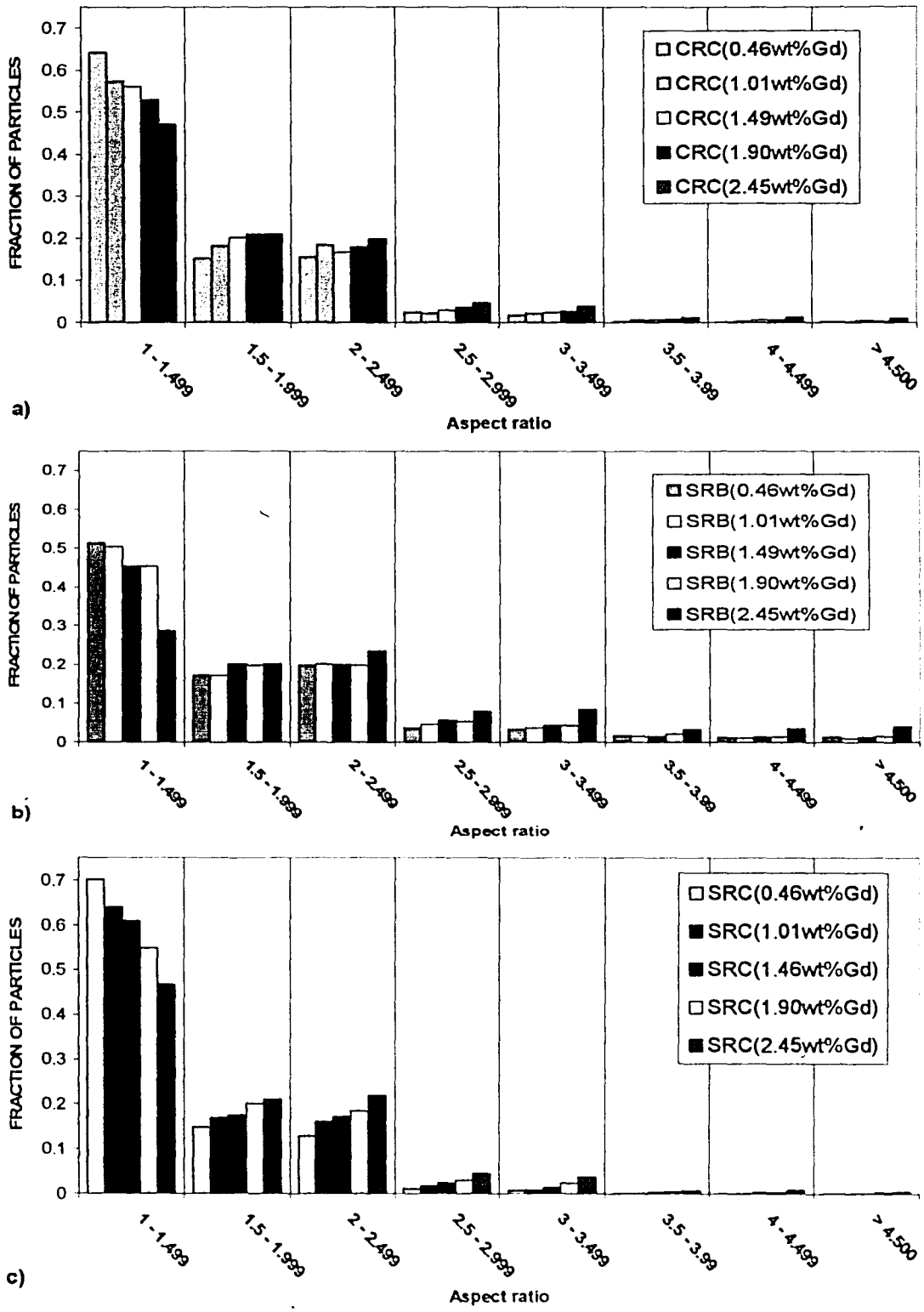

Figure 27: a) Aspect ratio histogram for the CR plates longitudinal to the primary rolling direction b) Aspect ratio histogram for the SR plates transverse to the rolling direction c) Aspect ratio histogram for the SR plates longitudinal to the rolling direction

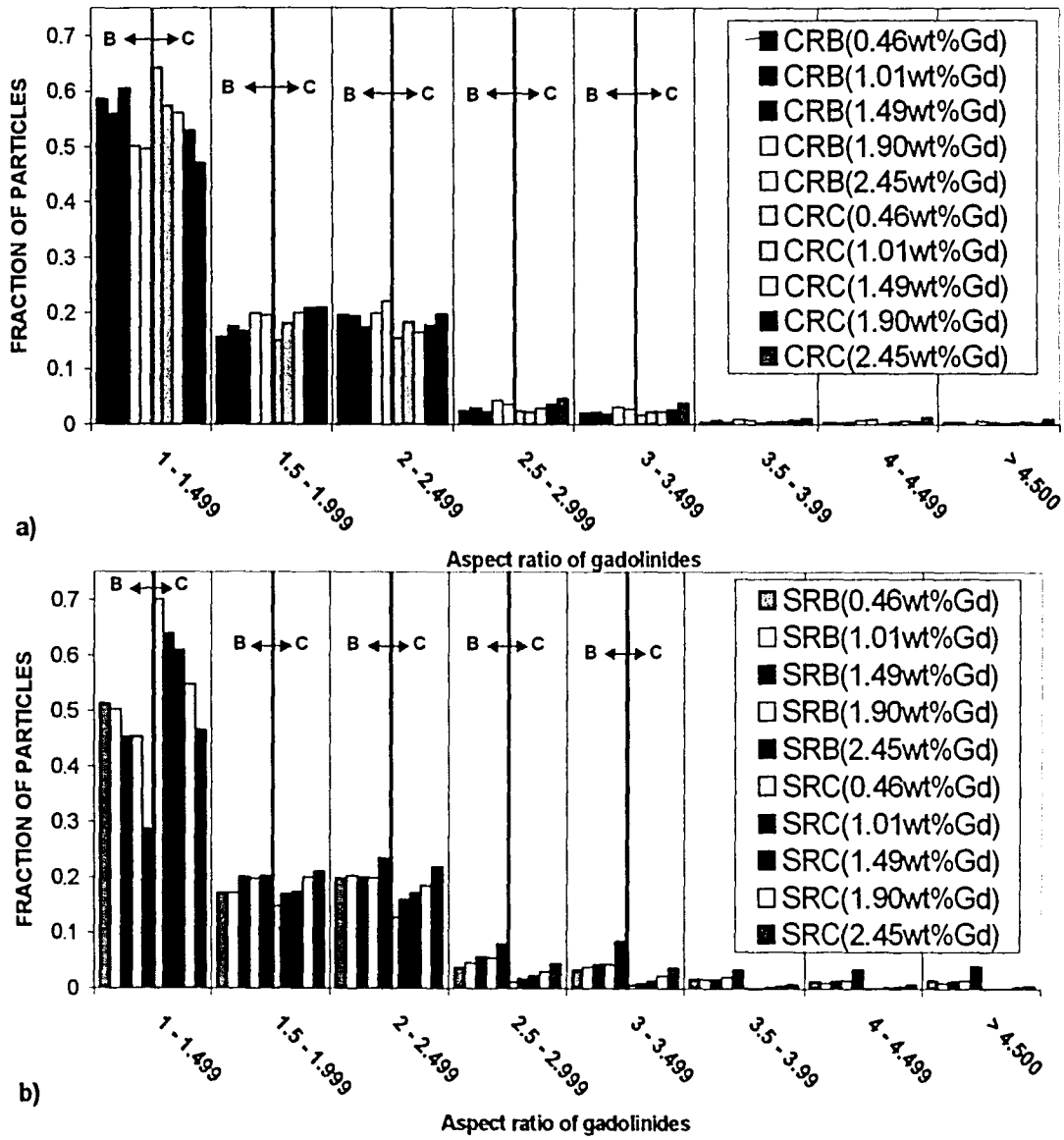

Figure 28: a) Aspect ratio histogram comparing the CR plates transverse to the primary rolling direction to the CR plates longitudinal to the primary rolling direction. b) Aspect ratio histogram comparing the SR plates transverse to the rolling direction to the SR plates longitudinal to the rolling direction

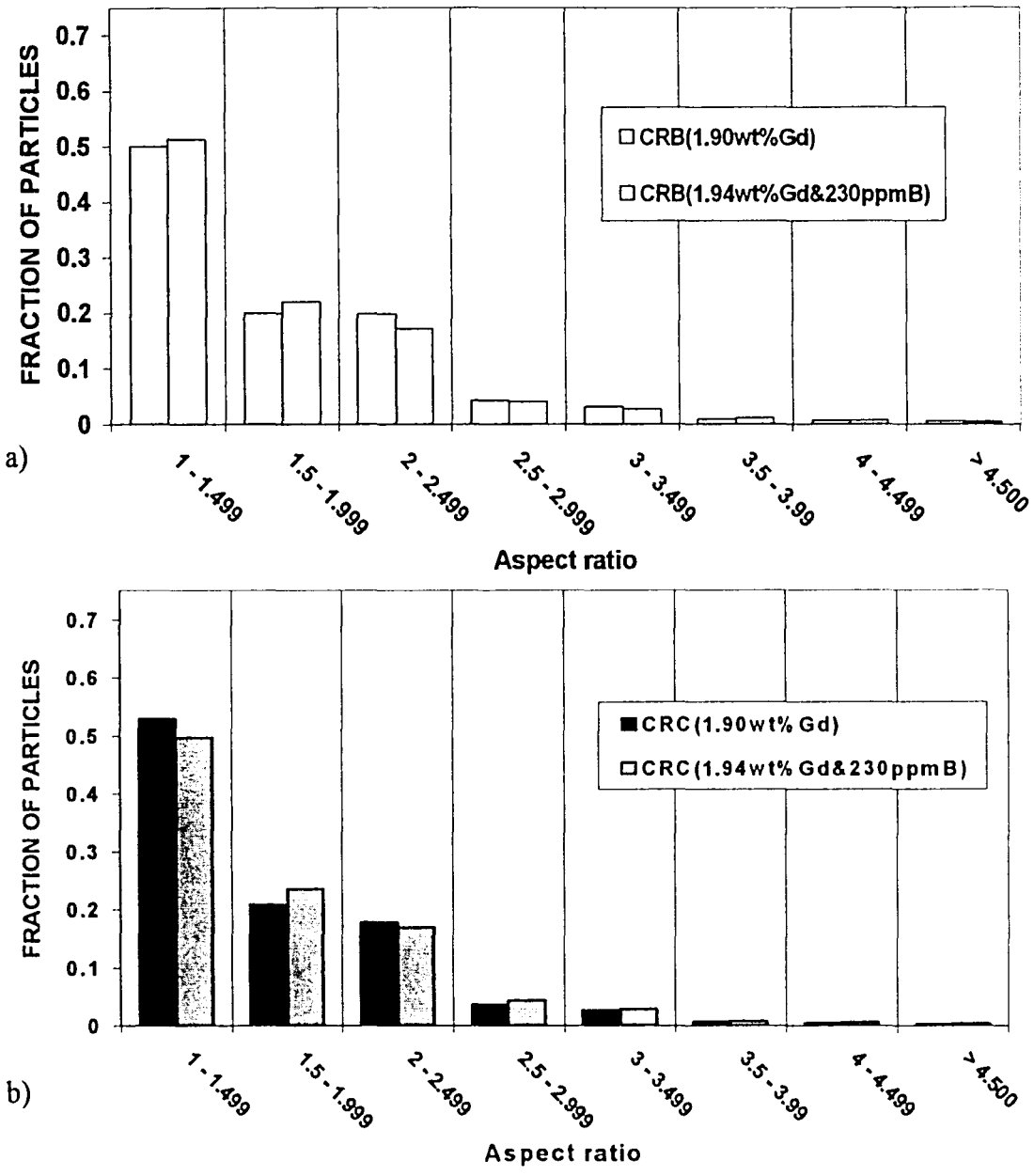

Figure 29: a) Aspect ratio histogram comparing the CR plates in the B plane of the B containing alloy and the alloy containing the same concentration of Gd. b) Aspect ratio histogram comparing the CR plates in the C plane of the B containing alloy and the alloy containing the same concentration of Gd.

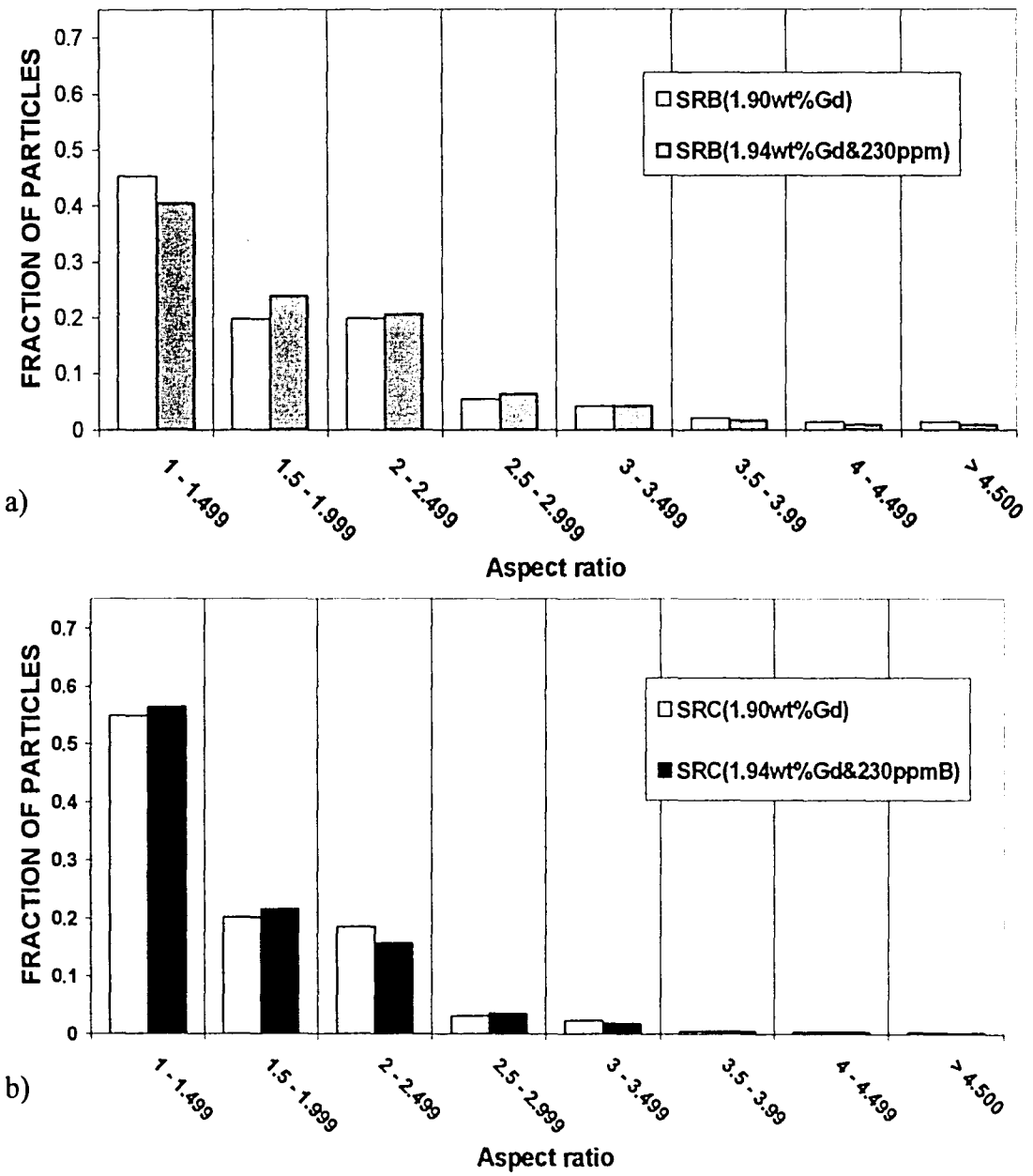

Figure 30: a) Aspect ratio histogram comparing the SR plates in the B plane of the B containing alloy and the alloy containing the same concentration of Gd. b) Aspect ratio histogram comparing the SR plates in the C plane of the B containing alloy and the alloy containing the same concentration of Gd.

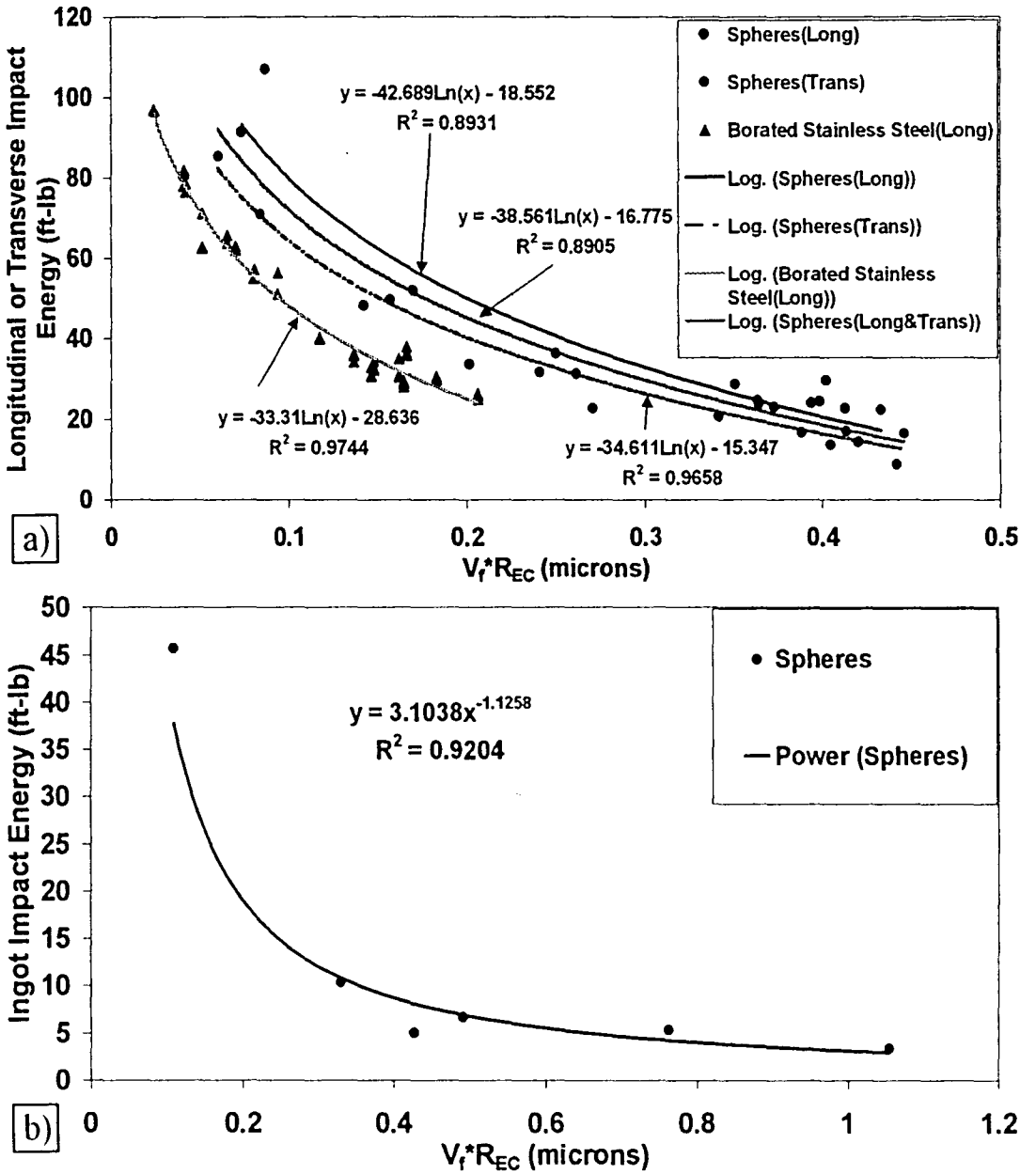

Figure 31: a) Plate Impact energies versus V_fR_{EC} parameter for BSS and Ni-Gd-Mo-Cr alloys b) Ingot impact energy versus V_fR_{EC} parameter for Ni-Gd-Mo-Cr alloys

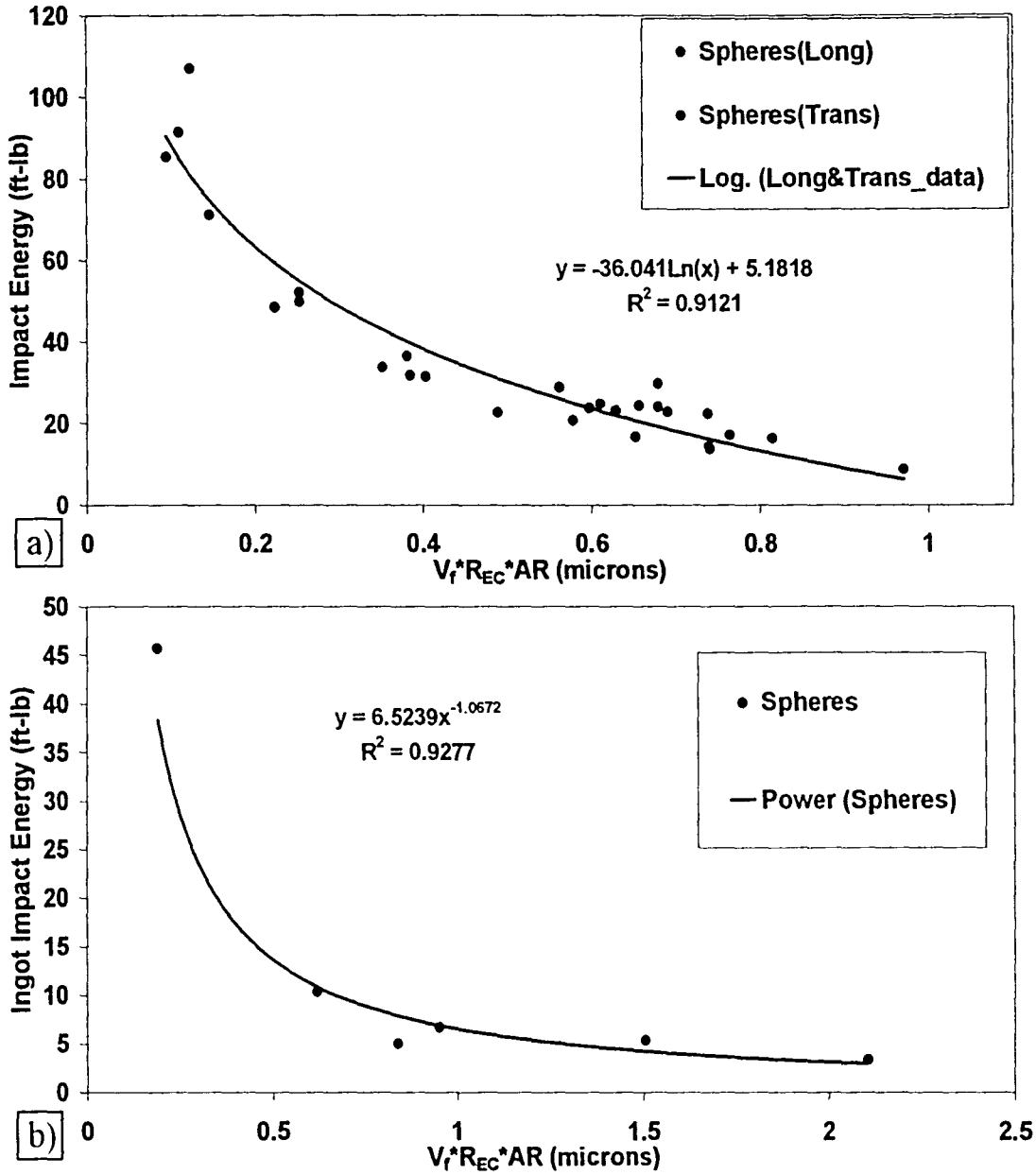

Figure 32: a) Plate impact energies versus $V_fR_{EC}AR$ parameter for Ni-Gd-Mo-Cr alloys b) Ingot impact energies versus $V_fR_{EC}AR$ parameter for Ni-Gd-Mo-Cr alloys

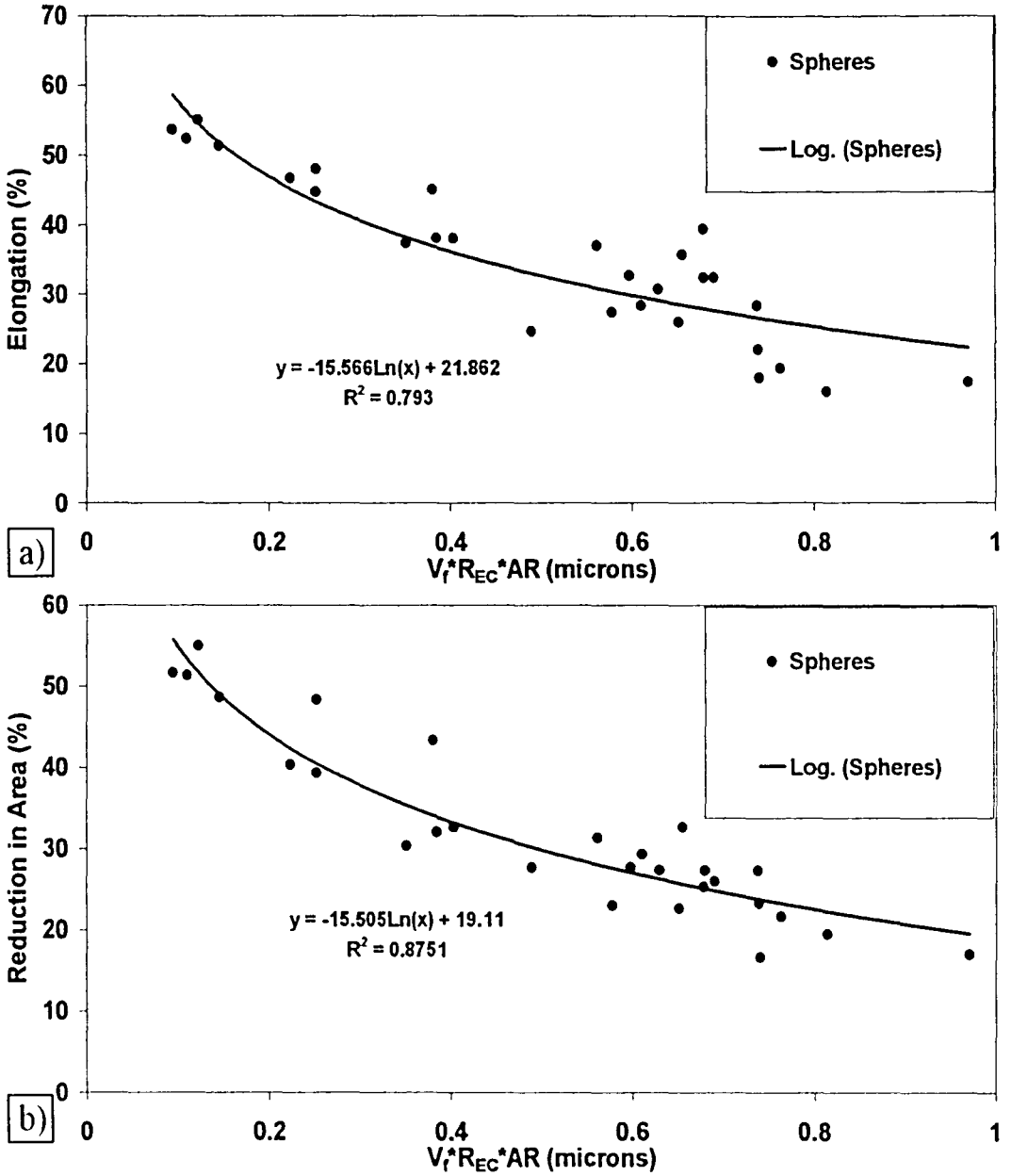

Figure 33: Elongation versus $V_f R_{EC} AR$ parameter for Ni-Gd-Mo-Cr alloys b) Reduction in Area versus $V_f R_{EC} AR$ parameter for Ni-Gd-Mo-Cr alloys

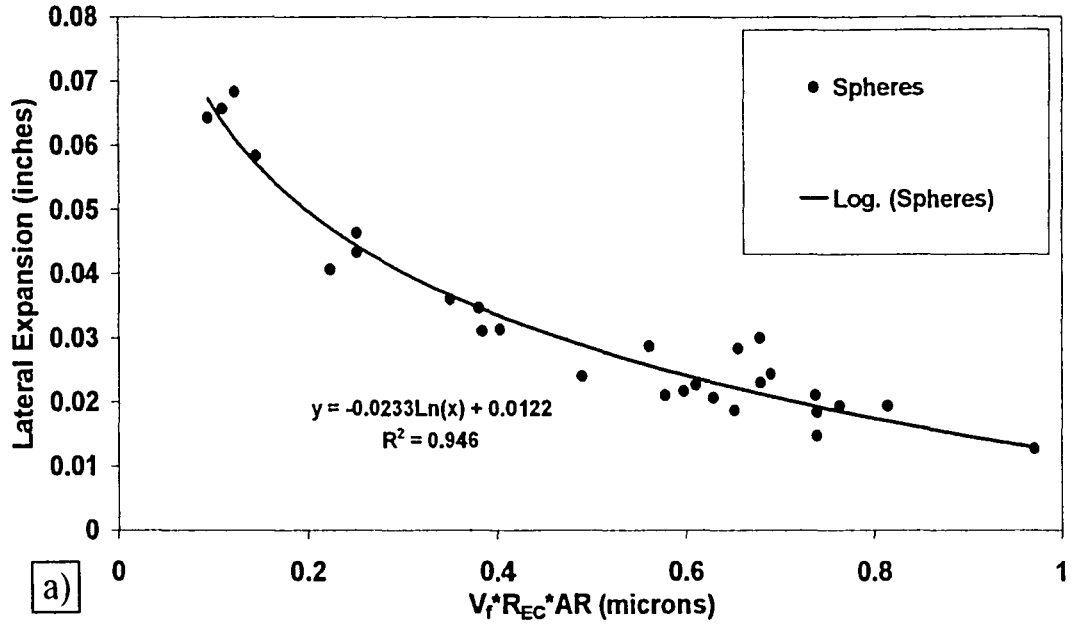

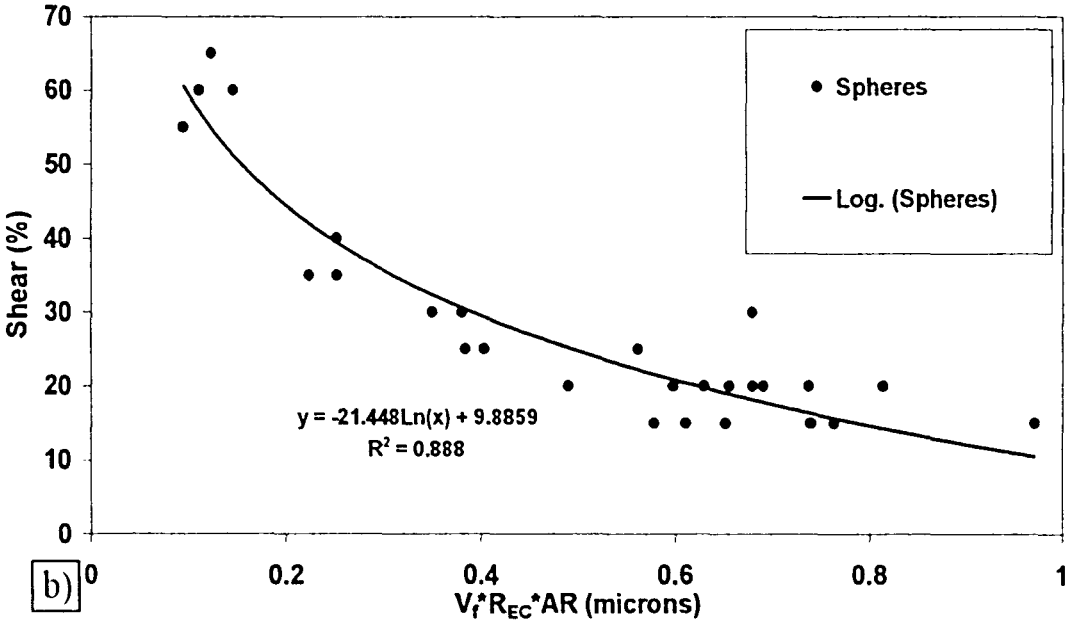

Figure 34: a) Lateral expansion versus $V_f R_{EC} AR$ parameter for Ni-Gd-Mo-Cr alloys
b) Shear percentage versus $V_f R_{EC} AR$ parameter for Ni-Gd-Mo-Cr alloys

Reference List

1. DuPont, J.N. et.al.: *Welding Journal*. Dec. 2004, **83**(12), pp. 319-329.

2. Q.G Wang: *Metallurgical and Materials Transactions*., December 2003, **34A**, pp. 2887-2899.

3. Dieter, G. E. *Mechanical Metallurgy*. New York, NY: McGraw-Hill Book Company, 1986.

4. W.H. Hunt, J.R. Brockenbrough, and P.E. Magnusen: *Scripta Metall. Mater.*, 1991,**25** (1), pp. 15-20.

5. DuPont, J.N. et.al.: *Welding Journal*. Nov. 2004, Vol. **83**(11), pp. 289s-300s.

6. ASTM E-23-98, Notched Bar Impact Testing of Metallic Materials, American Society of Testing and Materials, West Conshohocken, Pennsylvania.

7. ASTM E-8-00, Tension Testing of Metallic Materials, American Society of Testing and Materials, West Conshohocken, Pennsylvania.

8. ASTM E 92-82, Standard Test Method of Vickers Hardness of Metallic Materials, West Conshohocken, Pennsylvania.

9. ASTM E 1820-01, Standard Test Method for Measurement of Fracture Toughness, West Conshohocken, Pennsylvania.

10. ASTM E-1921-97, Standard Test Method for Determination of Reference Temperature, T_o, for Ferritic Steels in the Transition Range, American Society of Testing and Materials, West Conshohocken, Pennsylvania

11. Robino, C.V., and Cieslak, M.J.: *Metallurgical and Materials Transactions*., July, 1995, vol. **26A**, pp 1673-1685.

12. Development of Gadolinium-Containing Stainless Steels, January 2001 US Dep of Energy, DOE/SNF/REP-066 Rev.0

13. Hertzberg, Richard W. *Deformation and Fracture Mechanics of Engineering Materials*. New York: John Wiley and Sons, Inc, 1996.

14. Fullman, R.L., *Trans. Met. Soc. AIME*, 1953, **197**, pp. 447-452.

15. Corti, C.W. et.al., *International Metallurgical Reviews*, 1974, **19**, pp. 77-88.

16. Yang, J. et.al., *Acta Metallurgia et Materialia.*, Dec. 1990, **38**, pp. 2613-2619.

17. Popelar, C.H. et.al., *Experimental Mechanics.*, Dec. 2000, **40**, pp. 401-407.

18. Tomita, Y., *International Materials Review.*, 2000, **45**, pp. 27-37.

19. ASM Handbook: *Metals Handbook-Desktop Edition*, Second Edition, 1998, p.372

20. Robino, C.V., and Cieslak, M.J.: *CRADA #CR1042.*, February, 1994, pg. 80.

VITA

Michael Joseph Minicozzi was born on September 14, 1981 in Berkeley Heights, NJ to his parents Vincenzo and Carmelina. He was raised in Berkeley Heights until he graduated with honors in the spring of 1999 from Governor Livingston High School. Michael grew up with two older brothers, Donato, and Enzo. Michael began his college career in the fall of 1999 as an engineering student at Lehigh University. In the spring of 2003, Michael graduated magna cum laude with a Bachelors of Science Degree in Materials Science and Engineering. He then went on to become a graduate student in the Materials Science and Engineering Department in the fall of 2003.

END OF TITLE